

# HOT DIFFUSE EMISSION IN THE NUCLEAR STARBURST REGION OF NGC 2903

MIHOKO YUKITA<sup>1</sup>, DOUGLAS A. SWARTZ<sup>2</sup>, ALLYN F. TENNANT<sup>3</sup>, ROBERTO SORIA<sup>4</sup>, AND JIMMY A. IRWIN<sup>1</sup>

<sup>1</sup> Department of Physics and Astronomy, University of Alabama, Tuscaloosa, AL 35487, USA

<sup>2</sup> Universities Space Research Association, NASA Marshall Space Flight Center, ZP12, Huntsville, AL 35812, USA

<sup>3</sup> Space Science Office, NASA Marshall Space Flight Center, ZP12, Huntsville, AL 35812, USA

<sup>4</sup> International Centre for Radio Astronomy Research, Curtin University, GPO Box U1987, Perth, WA 6845, Australia

*Accepted to Astrophysical Journal*

## ABSTRACT

We present a deep *Chandra* observation of the central regions of the late-type barred spiral galaxy NGC 2903. The *Chandra* data reveal soft ( $kT_e \sim 0.2\text{--}0.5$  keV) diffuse emission in the nuclear starburst region and extending  $\sim 2'$  ( $\sim 5$  kpc) to the north and west of the nucleus. Much of this soft hot gas is likely to be from local active star-forming regions; however, besides the nuclear region, the morphology of hot gas does not strongly correlate with the bar or other known sites of active star formation. The central  $\sim 650$  pc radius starburst zone exhibits much higher surface brightness diffuse emission than the surrounding regions and a harder spectral component in addition to a soft component similar to the surrounding zones. We interpret the hard component as being also of thermal origin with  $kT_e \sim 3.6$  keV and to be directly associated with a wind fluid produced by supernovae and massive star winds similar to the hard diffuse emission seen in the starburst galaxy M82. The inferred terminal velocity for this hard component,  $\sim 1100$  km s<sup>-1</sup>, exceeds the local galaxy escape velocity suggesting a potential outflow into the halo and possibly escape from the galaxy gravitational potential. Morphologically, the softer extended emission from nearby regions does not display an obvious outflow geometry. However, the column density through which the X-rays are transmitted is lower in the zone to the west of the nucleus compared to that from the east and the surface brightness is relatively higher suggesting some of the soft hot gas originates from above the disk; viewed directly from the western zone but through the intervening disk of the host galaxy along sightlines from the eastern zone. There are several point-like sources embedded in the strong diffuse nuclear emission zone. Their X-ray spectra show them to likely be compact binaries. None of these detected point sources are coincident with the mass center of the galaxy and we place an upper limit luminosity from any point-like nuclear source to be  $< 2 \times 10^{38}$  erg s<sup>-1</sup> in the 0.5–8.0 keV band which indicates that NGC 2903 lacks an active galactic nucleus. Heating from the nuclear starburst and a galactic wind may be responsible for preventing cold gas from accreting onto the galactic center.

*Subject headings:* galaxies: evolution — galaxies: individual (NGC 2903), — galaxies: nuclei — X-rays: galaxies

## 1. INTRODUCTION

Stellar bars are common features of disk galaxies (Masters et al. 2011; Sellwood 1993; Buta 2011) where they efficiently channel gas into the central regions. The dynamics of bars is critical to galactic (pseudo)bulge growth and hence to evolution along the Hubble sequence (Kormendy & Kennicutt 2004) and to fueling central supermassive black holes (e.g., Shlosman et al. 1990) in isolated galaxies. In isolated late-type disk galaxies, stellar bars can efficiently transport gas into their central regions because of their relatively low bulge masses compared to early-type disks. Gas may accumulate at the ends of the bar before being driven inward by the gravitational torques within the bar (Combes & Elmegreen 1993). The gas forms thin “centered” dust lanes along the bar (Athanasoula 1992). There is less shear in the bars of late-type disks giving rise to substantial star formation along the bar.

There are often no central resonances in late-type disks, in contrast to bars in early-type disks; the bar extends to about the turn-over radius of the rotation curve, near the inner Lindblad resonance, and corotation occurs even further out in the disk (e.g., Shlosman 1999). In this case, accretion does not stall to form a circum-

nuclear ring but accumulates until self-gravity leads to burst-like episodes (Sarzi et al. 2007) of star formation – inflow may be impeded by stellar feedback but not by resonance phenomena as in early-type disks. Star formation and feedback can deplete the gas reservoir even at small distances beyond the sphere of influence of central black holes (Davies et al. 2010; Thompson et al. 2005) or, it may enhance fueling of black holes if the starburst occurs very near the central compact object (Watabe et al. 2008).

The study of structures such as bars and circumnuclear rings in X-ray light can directly reveal details that are hidden at many other wavelengths. The X-ray morphology not only helps to pinpoint locations of recent star formation but also traces high-pressure hot gas wind fluid that may quench star formation, impede accretion toward the galactic center, and drive energetic outflows. The best subjects for X-ray studies of these phenomena are isolated nearby galaxies inclined enough to distinguish galactic outflows while leaving the nucleus exposed to direct view and galaxies lacking strong active galactic nucleus (AGN) activity which could mask the fainter X-ray emission from circumnuclear star formation.

NGC 2903 is a nearby (8.9 Mpc,  $1'' = 43$  pc; Drozdovsky

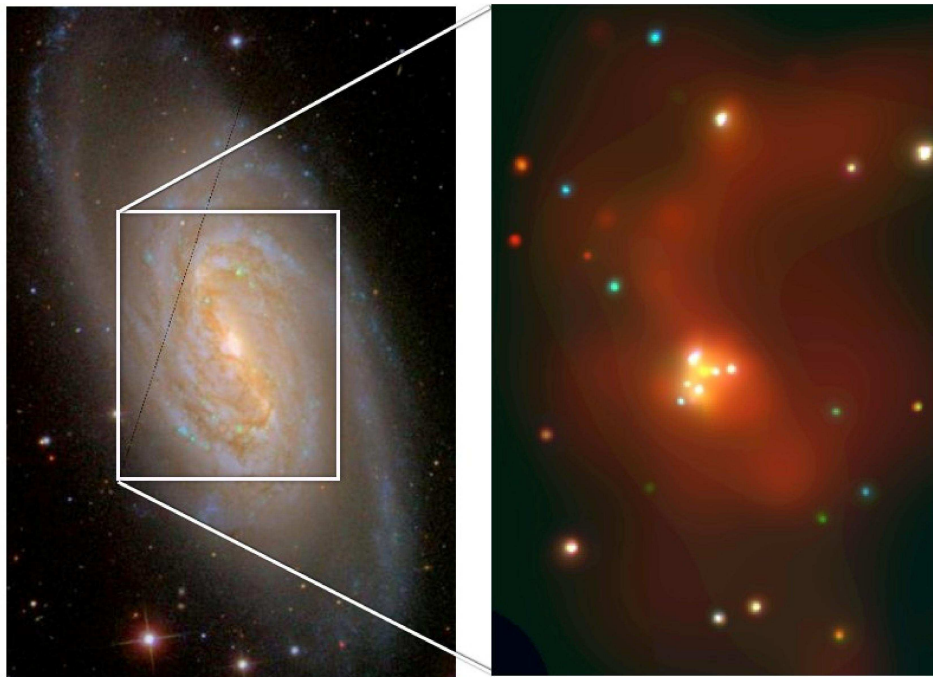


FIG. 1.— Left: the central  $4' \times 6'$  region of SDSS image. Blue, green, and red correspond to the  $g$ ,  $r$ , and  $i$  bands, respectively. Young stars in spiral arms are traced in blue, and bright HII regions appear in green. The complex dust lane structures along the bar and spiral arms are also noticeable in darker color. White box corresponds to the region shown in the right panel. Right: the central  $2' \times 3'$  region of *Chandra* image. Red, green, and blue correspond to the energy ranges, 0.5–1.0 keV, 1.0–2.0 keV, and 2.0–8.0 keV, respectively. The image is adaptively smoothed with a minimum signal-to-noise of 3.

& Karachentsev 2000) late-type barred SAB(rs)bc galaxy with strong circumnuclear star formation. NGC 2903 was first classified as having a central concentration of multiple bright hotspots superposed on a fainter background in an early galaxy classification scheme (Morgan 1958) based on central light morphologies (see also Sérsic & Pastoriza 1965, 1967). These hotspots have since been identified as young massive star clusters in optical and near-IR images interspersed with numerous bright HII regions (Planesas et al. 1997; Alonso-Herrero et al. 2001; Hägele et al. 2009) within an  $\sim 650$  pc diameter circumnuclear star-forming region. The star formation rate (SFR) in this region alone is  $\sim 0.7 M_{\odot} \text{ yr}^{-1}$  (Alonso-Herrero et al. 2001; Leon et al. 2008). This nuclear region is bright at wavelengths from X-rays (Tschöke et al. 2003; Pérez-Ramírez et al. 2010), UV (e.g., Popping et al. 2010), optical and mid-IR, to CO (Sheth et al. 2002; Helfer et al. 2003), HCN (Leon et al. 2008), and radio (Wynn-Williams & Becklin 1985; Tsai et al. 2006). For the most part, the nuclear region displays a patchy morphology with little obvious symmetry. Perhaps the precise center is best seen in high-resolution  $H$ -band images (e.g., Pérez-Ramírez et al. 2000; Alonso-Herrero et al. 2001) where a two-arm nuclear spiral pattern is also evident.

The nuclear region of NGC 2903 is clearly being fueled by inflow of gas along its bar (Hernandez et al. 2005; Leon et al. 2008). The total SFR along the bar is comparable to the rate in the nuclear region,  $\sim 0.7 M_{\odot} \text{ yr}^{-1}$  (Leon et al. 2008; Popping et al. 2010). The stellar bar extends roughly  $1'$  ( $\sim 2.5$  kpc) from the nucleus at a P.A. of  $24^{\circ}$  (Sheth et al. 2002). A strong, nearly unbroken dust lane along the bar is clearly visible in molecular bands (Sheth

et al. 2002; Leon et al. 2008). The dust lane leads the stellar bar (P.A.  $\sim 30^{\circ}$ , rotation is counterclockwise (CCW) and the disk is inclined  $\sim 60^{\circ}$ ) but trails active star formation visible as a curved string of numerous bright HII regions further downstream (Sheth et al. 2002; Popping et al. 2010; Knapen et al. 2002, see particularly Figure 1 of Sheth et al.). These offsets are expected inside the corotation radius when gas and dust dissipates energy and loses angular momentum as it passes through the stellar bar (e.g., Martin & Friedli 1997).

The bar is not as distinct at shorter wavelengths but instead appears patchy as does the outer flocculent spiral arm structure (Popping et al. 2010). The spiral pattern is clearest in HI maps (e.g., Walter et al. 2008). Deep images reveal an HI envelope extending to at least three times the optical diameter of the galaxy (Irwin et al. 2009) indicating no recent interactions which tend to truncate the HI disk (Higdon et al. 1998; Chung et al. 2009).

Hence, NGC 2903 is in many respects a textbook example of an isolated late-type barred spiral galaxy displaying a gas-rich star-forming nucleus and bar structure. This makes the galaxy an ideal target to study gas flow driven by the internal structures. Here we investigate the properties of the X-ray emitting hot gas and point-like sources in NGC 2903 revealed by a deep *Chandra X-ray Observatory* spectrophotometric image. We mapped X-ray emission in order to examine the correlation of the hot gas and point sources with sites of current star formation and of the various galactic structures in § 2. The detailed properties of the hot gas is analyzed in § 3, where we do confirm the emission asymmetry in the diffuse X-ray light first revealed by *ROSAT*/PSPC images (Tschöke et al. 2003) and visible in contemporary *XMM*-

*Newton* data (Pérez-Ramírez et al. 2010). We search for an nuclear activity in § 4 and find that none of the point sources are coincident with the nucleus of the galaxy. We discount the possibility of a low-luminosity AGN in NGC 2903 (cf. Pérez-Ramírez et al. 2010). We discuss that some of this emission likely traces a galactic wind or fountain extending above the disk of NGC 2903 originating in the nuclear hotspot region and revealing active stellar feedback and its influence on the growth of nucleus in § 5.

## 2. MAPPING THE X-RAY EMISSION FROM NGC 2903

NGC 2903 was observed with *Chandra* using the ACIS-S instrument in imaging mode on 7 March 2010 (ObsID 11260). The level 1 event list was reprocessed using the CIAO (version 4.3) tool *acis\_process\_events* to apply the CTI correction and to adjust for the time-dependent gain (with CALDB 4.3.0). Then, bad and hot pixels as well as bad status bits and grades were filtered out to create a level 2 event file. In order to identify any background flares, a lightcurve, binned to 500 s increments, was created from events in the energy range of 10–12 keV where the telescope mirrors were insensitive to X-rays. Background flares were identified and removed using the  $3\sigma$  clipping method<sup>1</sup> which resulted in 92 ks of the final GTI for this observation. The angular resolution of the *Chandra* mirrors is slightly better than the pixel resolution of the ACIS detector. Hence, we created a subpixel resolution image in the nuclear region by applying the sub-pixel event-repositioning algorithm “EDSER” of Li et al. (2004), which became available in CIAO v.4.3. For the rest of the galaxy, the standard  $0''.49$  pixel resolution image was created.

X-ray emission in star-forming galaxies like NGC 2903 arises from various sources including bright X-ray binaries (appearing as relatively hard point-like sources), diffuse hot gas from supernovae and massive star winds, and underlying emission from numerous fainter unresolved X-ray binaries. Figure 1 displays a  $4' \times 6'$  3-band optical image of NGC 2903 obtained from the Sloan Digital Sky Survey (York et al. 2000) along with a 3-color smoothed X-ray image of the central  $2' \times 3'$  region. The X-ray image shows numerous point-like sources as well as high surface brightness relatively hard diffuse emission in the nuclear region and more extended and softer diffuse emission throughout much of this central region of NGC 2903. In this section, we first characterize the bright detected point sources and then describe the morphology of the diffuse emission and create maps of the thermodynamic state of the hot gas from which we identify larger zones that we analyze spectroscopically in § 3.

### 2.1. X-Ray Point Sources

The source finding tool in *lextract* (Tennant 2006) was applied in the energy range of 0.5–8.0 keV to detect point sources inside the  $D_{25}$  isophote. A total of 92 point-like sources were detected with a signal-to-noise ratio (S/N) above 2.4 (see Tennant 2006) and with a minimum of 5 counts above the background uncertainty. These sources are tabulated in the Appendix where we also provide spectral analysis of the brightest sources. A spectrum obtained by co-adding events from all sources was

also examined. Its rough spectral shape is that of an absorbed power law with spectral index  $\Gamma = 1.95 \pm 0.02$  although there are some large fit residuals in the  $\sim 1$ –2 keV range likely due to contributions from (point-like) thermal emission sources. The total luminosity in point sources is  $1.9 \times 10^{40}$  erg s<sup>−1</sup> in the 0.5–8.0 keV range.

Visual inspection of the point source locations overlaid on the *GALEX* UV, SDSS optical, *Spitzer* near-IR, and the BIMA CO images revealed very few correlations with features visible at these other wavelengths. The notable exceptions are (1) the nuclear region which contains 8 point-like X-ray sources within a  $15''$  (650 pc) radius (this region was unresolved in previous *XMM-Newton* and *ROSAT* X-ray observations) and (2) a bright object north of the nucleus, designated CXOUJ093209.7+213106, coincident with strong emission from the UV to mid-IR bands.

We note that there is also strong, relatively hard, diffuse emission extending throughout the nuclear region. Some detected point sources in the nuclear region may be knots of hot gas rather than X-ray binaries traditionally associated with point-like sources. We inspected the X-ray colors and sizes of these sources to help differentiate compact binaries from concentrations of hot gas following the simple methods in Swartz et al. (2006). For the latter, we applied two-dimensional Gaussian models to the distribution of X-ray events to determine if sources are point-like indicating compact binaries or more extended hot gas concentrations. None of the 8 point-like sources in the nuclear region were conclusively identified as having a thermal origin. Further analysis of the point sources and diffuse emission in the central  $15''$  region is deferred to § 4.

### 2.2. Diffuse X-Ray Emission

We confine our analysis of the diffuse X-ray emission in NGC 2903 to the  $2' \times 3'$  region shown in the right panel of Figure 1. There is no evidence of diffuse emission beyond this region in either the *Chandra* or the recent *XMM-Newton* observations. A point-source-free diffuse emission map was created by removing the detected point sources and then filling the excluded regions by sampling the Poisson distribution of the mean levels of their local backgrounds using the CIAO tool *dmfilth*.

Figure 2 shows this diffuse emission map in the soft (0.5–2.0 keV) X-ray band. This emission map has been smoothed with the CIAO tool *aconvolve* using a Gaussian smoothing function with a width of 10 pixels ( $\sim 5''$ ). Also shown for comparison is an unsmoothed image binned by 4 pixels ( $\sim 2''$ ) which is the pixel scale used below for building maps of the thermodynamic state of the gas. Diffuse emission is clearly present in the central region. The low surface brightness diffuse emission extends to a few minutes of arc, especially to the north of the nucleus.

#### 2.2.1. Galactic Structures and X-Ray Morphology

Figure 3 shows the same  $2' \times 3'$  region as Figure 2 in different wavelength images: *HST*/ACS F814W, *GALEX* FUV, *Spitzer* 24  $\mu$ m, and BIMA SONG CO. The contours of the smoothed X-ray diffuse emission from Figure 2 are overlaid on each panel of Figure 3 to compare the diffuse X-ray emission to the galactic structures and star-forming regions visible at these other wavelengths.

<sup>1</sup> <http://cxc.harvard.edu/ciao/threads/flare/>

The brightest feature at all wavelengths is the nuclear region. The bar is also clearly represented in the *HST*/ACS F814W image tracing the stellar emission and in the CO and 24  $\mu\text{m}$  images tracing cold molecular gas and dust. Popping et al. (2010) and Sheth et al. (2002) report an offset between these stellar and cold gas/dust bars and the  $\text{H}\alpha$  emission tracing young high-mass stars with the  $\text{H}\alpha$  emission *leading* the CCW-rotating bars. The UV image, tracing stars younger than  $\sim 100$  Myr, appears much more spotty and does not follow the bar structure. Popping et al. (2010) also note the UV emission is patchy and does not correlate well with either the  $\text{H}\alpha$  or 24  $\mu\text{m}$  tracers of current star formation. Instead, they find extremely young ages ( $< 10$  Myr) for UV-emitting clusters along the bar and much older ( $> 100$  Myr) for other clusters in the field. At the longer wavelengths, the emission extends beyond the ends of the bar into the trailing spiral arms and forms a distinct, though patchy, S-shaped pattern.

The highest surface brightness X-ray emission also occurs in the central region of NGC 2903. There is also weaker emission extending beyond the nucleus in the X-ray image but, except for a few bright knots, the emission is not confined to the stellar or molecular bar nor the S-shaped pattern visible in the IR and CO bands. Instead, this low surface brightness emission extends to the northwest of the nucleus as if filling the inner portion of the upper half of the S-shaped region of star formation traced by the 24  $\mu\text{m}$  emission. Contrary to this, there is no bar-like morphology along the southern half of the bar nor extended emission in the southwest S-shaped region in X-ray. We considered a difference in the column density might account for this asymmetry; however, no large difference in extinction between the north and south halves of the bar is reported from  $\text{H}\alpha$  or 24  $\mu\text{m}$  analysis (Popping et al. 2010). In summary, besides the nuclear region and a few isolated extended knots which may be associated with bright star-forming regions, there are no strong correlations between the X-ray morphology and the galactic structures seen at various other wavelengths.

### 2.2.2. X-Ray Thermodynamics Maps

The lack of strong correlations between diffuse X-ray emission surface brightness and galactic structures visible at other wavelengths prompted us to examine other properties of the diffuse X-ray emission in greater detail. To this end, we created maps of the thermodynamic state of this hot gas to examine if we see any particular morphological features in the X-ray properties.

Specifically, we created a point-source-free image binned by 4 pixels ( $\sim 2''$ ). Then, we extracted a spectrum from a circular region around each pixel in the binned image. This procedure follows the method described in Randall et al. (2008), who employed the technique of O’Sullivan et al. (2005) and Maughan et al. (2006). The radius of each region was chosen to contain at least 500 counts after background subtraction. A region to the northeast outside of the  $D_{25}$  annulus was used for the background. We constrained the maximum radius of each region to be  $\leq 30''$ ; we discard regions needing  $> 30''$  to contain  $> 500$  net counts. Overall, the resulting range of radii is  $5''$ – $30''$ . This is much larger than the pixel scale representing the resulting parameter values; this

is in a sense equivalent to “smoothing” the parameter maps.

Each spectrum is then fitted using the energy range between 0.5–2.0 keV, because there are very few counts detected above 2 keV after the background subtraction. We fitted with an absorbed collisionally ionized optically thin plasma model, namely **phabs\* mekal** in XSPEC.<sup>2</sup> Due to low counts in each spectrum, we use Poisson statistics to fit spectra and we fixed the metallicity to the solar value following the *XMM-Newton* Reflection Grating Spectrometer (RGS) analysis of Pérez-Ramírez et al. (2010); see also Pilyugin et al. (2004) and references therein. Applying the same model to the spectra of each spatial region allows us to spatially resolve relative changes in the thermodynamic properties of the gas.

Figure 4 shows the resulting X-ray temperature,  $kT_e$ , absorbing column density,  $N_H$ , electron density,  $n_e$ , and pressure,  $P$ , maps of the hot gas over the same regions as displayed in Figure 2. We also overlay the *HST*/ACS F814W contours in order to visualize the underlying galactic structures.

The measured temperature shown in Figure 4 ranges from 0.2 to 0.3 keV with errors of 0.03 keV on average. This is a typical temperature for hot gas (0.1–0.7 keV) in star-forming regions in normal or starburst galaxies (e.g., Tyler et al. 2004; Strickland et al. 2004). The nuclear starburst region has relatively higher  $kT_e$  than the surrounding areas. The highest temperature in the nuclear region (yellow in the figure) is elongated in a roughly NW to SE direction nearly perpendicular to the bar and extending to the NW. This extension to the northwest is also seen in the *XMM-Newton* image presented in Pérez-Ramírez et al. (2010). However, there is no large difference in temperature among these regions overall, which is also consistent with what has previously been found in the other star-forming galaxies (e.g., Swartz et al. 2006; Wang et al. 2009). Interestingly, the temperature along the (northern) bar decreases whereas the surface brightness remains roughly constant. The temperature is higher to the northwest of the northern bar (within the S-shape).

The measured  $N_H$  is in the range of  $(2\text{--}8) \times 10^{21} \text{ cm}^{-2}$ , which is much larger than the Galactic  $N_H$  value of  $3 \times 10^{20} \text{ cm}^{-2}$  (Dickey et al. 1990) along the line of sight. In fact, this is larger than the intrinsic  $N_H$  value for NGC 2903 of  $\sim 5 \times 10^{20} \text{ cm}^{-2}$  derived from the HI Nearby Galaxy Survey data (Walter et al. 2008) estimated using their Equation (5). We note that applying a single temperature model to the multi-temperature gas seen in galaxies often tends to result in a higher column density because of the need to suppress low-energy emission in the model (e.g., Yukita et al. 2010). Due to the low fitted model temperatures, the  $N_H$  uncertainties are somewhat large, about  $\pm (0.5\text{--}1.0) \times 10^{21} \text{ cm}^{-2}$ . The nuclear region and the dust lane to the east of the nucleus have the highest  $N_H$ . The north side of the bar also shows a relatively higher column density, and the regions to the west of the nucleus, where fewer and weaker dust lanes are visible in the optical *Hubble Space Telescope* (*HST*) image,

<sup>2</sup> The **mekal** model was used here because the solution is computed “on-the-fly” as opposed to being pre-defined on a finite model parameter grid as does the **apex** model so that it does not suffer from a discretization problem.

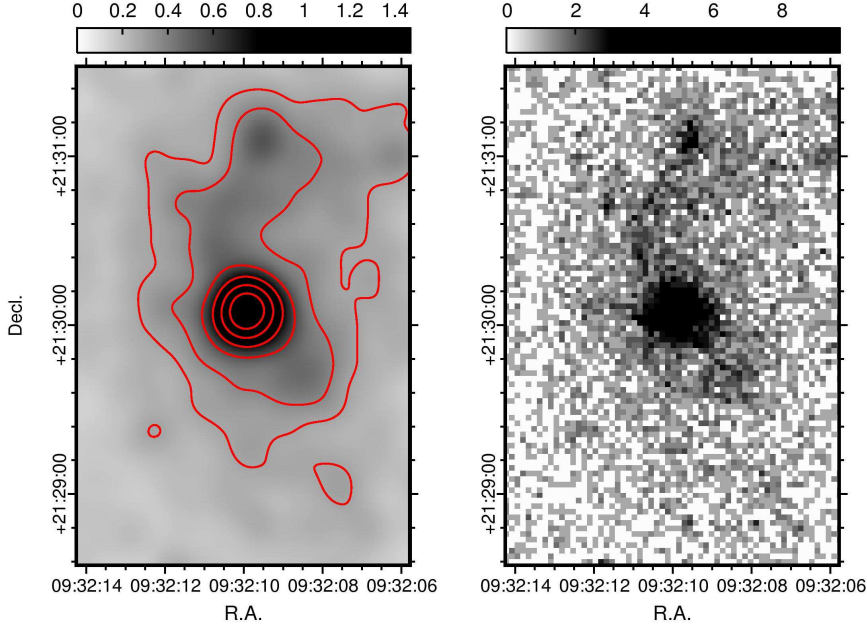


FIG. 2.— Left: the central  $2' \times 3'$  of the point source-free X-ray soft (0.5–2.0 keV) diffuse emission map. The image was smoothed using the *CIAO* tool, *aconvolve* with Gaussian  $\sigma$  width of  $5''$ . The contours are also plotted in square root scale, specifically 0.075, 0.132, 0.307, 0.59, 1.0 and 1.52 count pixel. The pixel scale of this image is  $0''.492$ . Right: the same as the left image, besides binned by  $2''$  scale rather than smoothed. The color bars for the both images indicate the square root of the intensity with the unit of count.

have relatively lower  $N_H$  values. However, the spectral properties, both  $N_H$  and  $kT$ , along the south side of bar does not show a correlation with the underlying galactic structures, similar to the lack of correlation with these features in the X-ray surface brightness.

The X-ray electron density,  $n_e$ , is estimated from the model fit parameters in the following way. The spectral model normalization,  $K$ , is related to the emission integral,  $\int n_e n_H dV \sim n_e^2 fV$ , where  $V$  is the X-ray emitting volume and  $f$  is a volume filling factor. This volume filling factor represents the fraction of the volume actually occupied by X-ray emitting gas. We assume that the number densities of ions,  $n_i$ , and electrons are equal. This is a reasonable assumption for hydrogen dominated plasma. The electron number density, then, can be estimated as  $n_e^2 \propto K/(fV)$ .

In order to derive an electron density map, we assume that the hot gas fully occupies ( $f \equiv 1$ ) a cylindrical volume represented by a scale height,  $h = 200$  pc, of the disk. The electron density then scales linearly with  $(fh)^{-1}$ . This is, of course, not the only possible scenario; the gas (or some fraction of the gas) may extend above the disk in the form of an outflow. This possibility is examined further in § 5.

Using the derived  $n_e$  and the flux-weighted mean X-ray temperature  $T_e$ , the hot gas pressure  $P/k = 2n_e T_e$  can be derived. The pressure is also highest in the nuclear region, approaching  $25 \times 10^5$  K cm $^{-3}$ , and is more centrally-peaked than either the temperature or the electron density alone. The pressure distribution is smoother beyond the nuclear region approaching a roughly constant value of  $(5-7) \times 10^5$  K cm $^{-3}$ .

In summary, Figure 4 shows that the highest density, temperature, and pressure region is the nuclear starburst region. This is also the highest surface brightness region

(Figure 2). The density is relatively high in the region along and to the northwest of the northern portion of the stellar bar. We do not see an analogous feature corresponding to the south side of the bar. Lastly, the pressure map indicates that only the nuclear starburst region is highly pressurized if we assume an equal scale height for all the regions. In fact, it is possible that the hot gas is flowing out into a low density halo region, which would imply a different morphology of the gas volume than considered here.

We point out that the fitted column density and temperature parameters are often anti-correlated. There are low column density (blue) regions, where the temperature is high (yellow and orange regions west of the nucleus). Also, the temperature is lower (red) where the column density is higher (yellow). Another, though weaker, positive correlation sometimes occurs between column density and electron density (proportional to the square root of the model normalization) in these single-temperature models. We show the column density of all the pixels in the map against their corresponding temperature to examine this behavior in Figure 5.

The left panel of Figure 5 clearly shows that most regions follow the anti-correlation with higher  $N_H$  values tending to correspond to lower temperatures. These regions are located in the bottom left side of the figure. There are also regions that do not follow this trend, spreading into the top right of the plot. We selected three groups in this parameter space as indicated by lines in the left panel of Figure 5 based on the grouping of the regions apparent to the eye. The right panel of Figure 5 shows the spatial map of the corresponding groups defined in this way. As anticipated, the nuclear region corresponds to the top right group consisting of the hottest, most heavily absorbed gas with clearly dif-



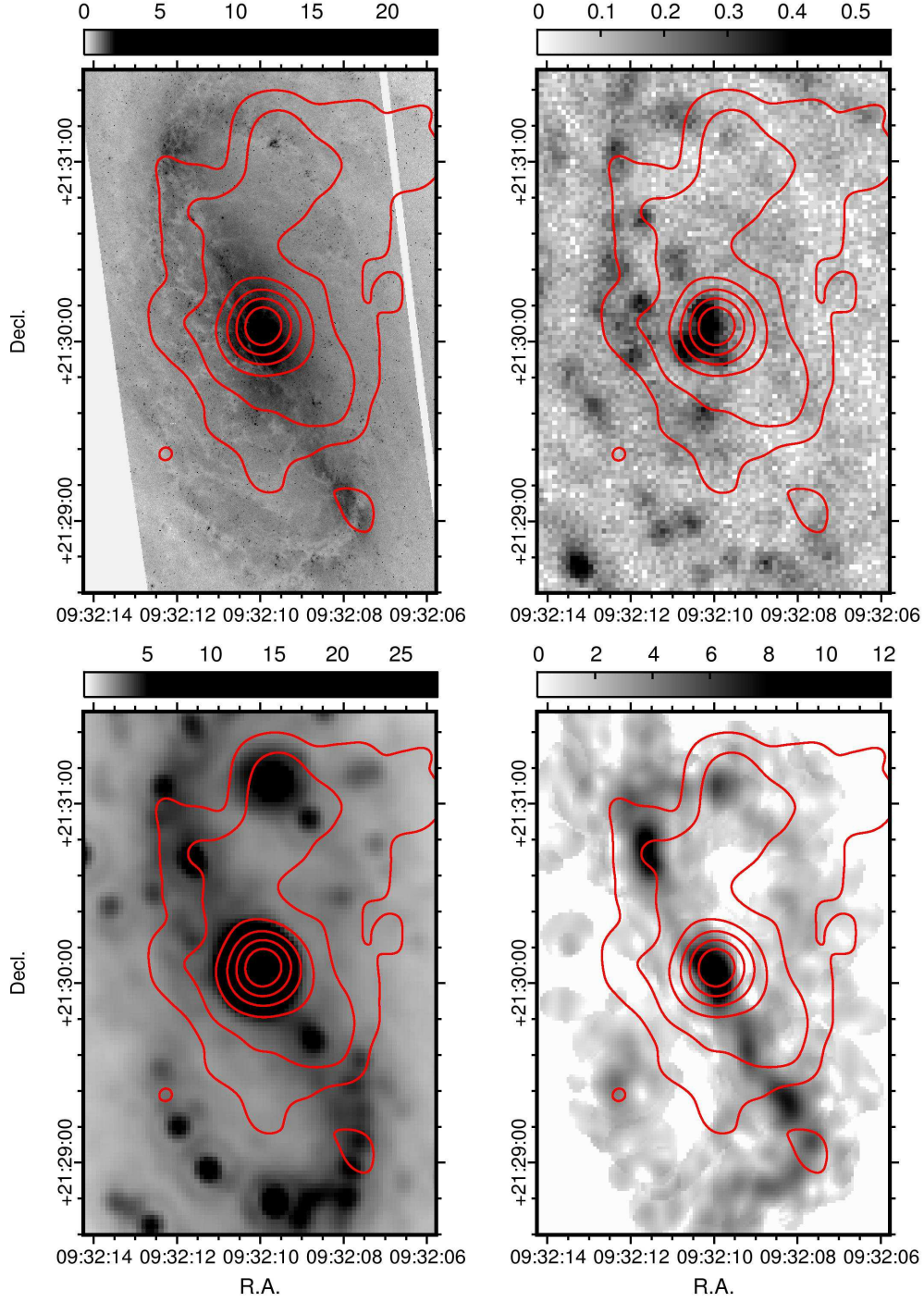


FIG. 3.— Central  $2' \times 3'$  of the NGC 2903 of *HST*/ACS F814W (top left), *GALEX* FUV (top right), CO (bottom right), and *Spitzer*  $24 \mu\text{m}$  (bottom right) images. The color bars indicate a square root of intensities. The *HST* image has the pixel scale of  $0''.05$  and the intensity unit of electron;  $1e$  corresponds to a fluence of  $7.1 \times 10^{-20} \text{ erg cm}^{-2} \text{ \AA}^{-1}$ , that is a specific flux  $F_\lambda = 1.0 \times 10^{-22} \text{ erg s}^{-1} \text{ cm}^{-2} \text{ \AA}^{-1}$ . The pixel scale of the *GALEX* FUV image is  $1''.5$  with the intensity units of counts  $\text{s}^{-1}$ . The BIMA SONG CO image has the pixel scale of  $1''$ . The unit of image is  $\text{Jy (beam)}^{-1} \text{ km s}^{-1}$ . The *Spitzer*  $24 \mu\text{m}$  image has the pixel scale of  $1''.5$ , and the map intensity is in  $\text{Jy sr}^{-1}$ . The contours depict the intensity of the smoothed X-ray diffuse emission shown the left panel of Figure 2.

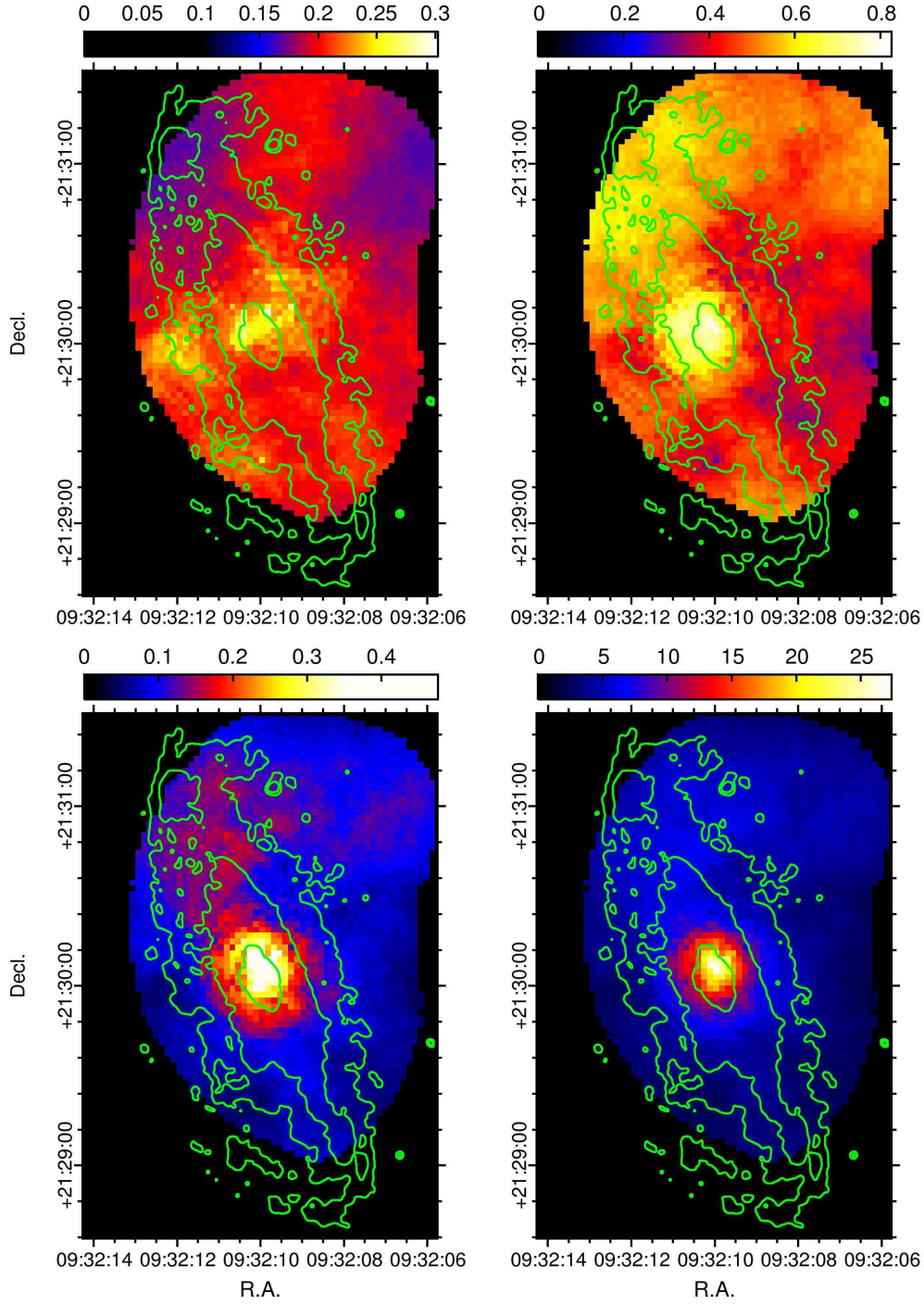


FIG. 4.— Same region as in Figure 2 of the temperature (top left), hydrogen column density (top right), electron density (bottom left), and pressure (bottom right) of the hot gas derived by applying an absorbed single temperature model (see the text). The units for each map are in keV,  $10^{22} \text{ cm}^{-2}$ ,  $\text{cm}^{-3}$ , and  $10^5 \text{ K cm}^{-3}$ , respectively, as denoted by the color bar at the top of each panel. One pixel corresponds to  $\sim 2''$ , which is the same as the right panel of Figure 2. However, the spectral extraction regions used to define the pixel values are larger than  $2''$ , see the text for details. The regions which did not contain enough counts for spectral fitting appear black. We note that a single temperature model can result in higher  $N_{\text{H}}$  and normalization, therefore resulting in a higher density. In order to compare with the galactic structures, the *HST*/ACS F814W contours are overlaid in green.

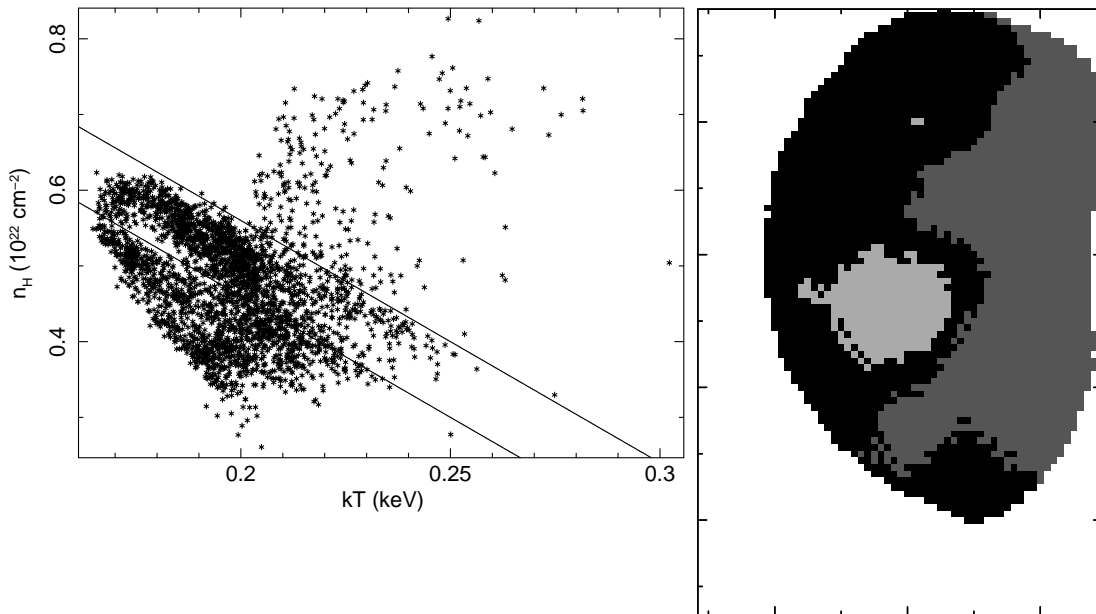


FIG. 5.— Left: The  $N_{\text{H}}$  vs.  $kT_e$  plot for the fits of an absorbed single temperature model using 0.5–2.0 keV. In general, there is an anti-correlation between  $N_{\text{H}}$  and  $kT_e$ , as a higher  $N_{\text{H}}$  results in a lower  $kT_e$  value. We divided the parameter space into 3 groups as indicated with straight lines. Right: the three parameter groups defined in the left panel are mapped in spatial coordinates. The light gray zone indicates the right top group, and the dark gray zone depicts the bottom left group, and the black zone is the middle group in the left panel. These two plots show that the nuclear region has both high  $N_{\text{H}}$  and  $kT_e$  values that do not follow the correlation seen in the rest of region.

ferent properties than the other two regions. The middle and bottom left groups also show strong spatial correlations. The middle group regions are located to the east and the bottom left group are located primarily to the west of the nuclear region.

Although these regions were found using solar abundances, we note that similar structures are evident when changing abundances to a different value, such as  $Z = 0.05 Z_{\odot}$ . In order to understand why these regions are different, we analyze the X-ray spectra extracted from these three groupings, or zones, where we are able to apply more complex models in the next section.

### 3. FURTHER SPECTRAL ANALYSIS OF THE DIFFUSE EMISSION

We have shown in the previous section, using detailed maps of the thermodynamic state of the hot, X-ray-emitting gas, that the spatial complexity observed at other wavelengths is clearly present at X-ray energies. On the other hand, there are no strong correlations between the X-ray morphology and the underlying galactic structure with the notable exception of the nucleus. There is a general trend of lower temperature and lower column density to the west of the nuclear region relative to east of the nuclear region. In this section, we will analyze in greater detail the spectral properties of three zones: the  $\sim 15''$  nuclear starburst region, and the two extended diffuse emission regions to the east and to the west of the nucleus.

#### 3.1. The Nuclear Zone

We performed X-ray spectral analysis of the diffuse nuclear emission defined as the light gray zone of Figure 5 from the  $N_{\text{H}} - kT_e$  correlation. This zone is roughly  $15''$  (650 pc) in radius. We first fit the same absorbed thermal model using the same energy range (0.5–2.0 keV)

as before to validate the results in our thermodynamic maps. We obtained  $N_{\text{H}} = 5.8^{+0.4}_{-0.3} \times 10^{21} \text{ cm}^{-2}$ , and  $kT_e = 0.22^{+0.01}_{-0.01} \text{ keV}$ , which is consistent with the results from the maps. However, with many more counts in the source spectrum, this simple absorbed thermal model with a solar abundance is not well fitted to the data ( $\chi^2_{\nu} \sim 4$ ).

In fact, there are enough counts to extend the model fit to higher energies, 0.5–6.0 keV, resulting in  $2205 \pm 48$  net counts after background subtraction. The same local background, taken from outside the  $D_{25}$  isophote, that was used for creating the thermodynamic map was used here. The spectrum was grouped to contain at least 40 counts in each spectral bin, and the  $\chi^2$  statistic was used for determining the goodness of fit.

Including the higher energy photons resulted in raising the temperature ( $kT_e = 0.5$ ) and lowering the column density ( $2 \times 10^{21} \text{ cm}^{-2}$ ) of the best-fitting single-temperature model but the fit is unacceptable ( $\chi^2_{\nu} \sim 6$ ). Next, we allowed the elemental abundances in the `mekal` model component to vary keeping their ratios fixed to the solar ratios given by Anders & Grevesse (1989). This dramatically improved the fit to  $\chi^2_{\nu} \sim 1.9$  with one fewer degree of freedom and resulted in raising the best-fitting temperature to  $kT_e = 0.58 \text{ keV}$  and lowering  $N_{\text{H}}$  to  $3 \times 10^{20} \text{ cm}^{-2}$ .

The resulting abundances were subsolar,  $Z = 0.05 Z_{\odot}$ , which is inconsistent with the *XMM-Newton*/RGS result (Pérez-Ramírez et al. 2010) and is problematic if the hot gas originates from  $\alpha$ -element-rich core-collapse supernovae as expected. On the other hand, the widely-applied Weaver model (Castor et al. 1975; Weaver et al. 1977) of hot bubble formation predicts the majority of hot gas is mass-loaded from the surrounding cold clouds rather than coming from the metal-rich shocked supernovae gas. It is also known that a simplistic model some-



times gives very low abundances when applied to the relatively low CCD resolution imaging spectra (Weaver et al. 2000). Hence, we do not argue strongly that the resultant abundance estimate is realistic and decided to fix abundances at the solar value, consistent with Pérez-Ramírez et al. (2010), in the remainder of our analysis.

The fitting residuals indicate that the single-temperature model best fits the data only between 0.7 and 1.2 keV. Therefore, we added a second model component, either a power-law component or a second thermal model, to account for the softer and harder emission.

Adding a power-law model resulted in a significantly improved fit statistic ( $\chi^2_\nu \sim 1$ ). The power-law index is  $\Gamma=2.65$ . This value is similar to that found in the nuclear starburst regions of NGC 1365 (Wang et al. 2009) and NGC 5135 (Levenson et al. 2004). These authors interpreted this hard emission as unresolved point sources; however, the power-law slope is much steeper than the slope of the detected point sources in NGC 2903 ( $\Gamma \sim 1.95$ ; see the Appendix). Also, fitting only the data in the range 2 and 6 keV gives an even steeper index of  $\sim 4$ . We argue that the harder X-ray emission is unlikely to come from unresolved point sources and is instead a hotter thermal component.

Adding a second thermal component instead of a power law results in a  $\chi^2_\nu \sim 2$ , but not yet an acceptable fit. The two temperature model results in a second temperature of  $\sim 3$  keV, which may be interpreted as shocked gas directly associated with a “wind fluid” as observed in powerful starbursts like M82 (Strickland & Heckman 2007, 2009). This is a more realistic interpretation than the unresolved point source (power law) interpretation of the hard emission for the nuclear region of NGC 2903. To obtain a better fit statistic, however, a third thermal component is required. The resultant fitting parameters are tabulated in Table 1 where the errors are quoted at the  $1\sigma$  (68% confidence level). Figure 6 shows the spectrum of the nuclear region for this 3-temperature model illustrating the complex line structures due to O and Fe emission between 0.6–1.2 keV, Mg at 1.3 keV and Si at 1.8 keV as well as a hard continuum above 2 keV. Note the fit residuals indicate some of these line features are still poorly reproduced by this model with abundances fixed to their solar values. The two lower temperatures for this model are  $\sim 0.2$  and 0.6 keV, which are typical values for star-forming regions and the halos of starburst galaxies (Strickland et al. 2004; Yukita et al. 2010). This model results in a column density  $N_H=1.4 \times 10^{21} \text{ cm}^{-2}$ .

We also derived other physical properties of the hot gas from the spectral fits; namely, the electron density  $n_e$  and pressure  $P$ , derived in the same manner as in § 2.2.2. Again, we note that the assumed geometry and hence hot gas volume can introduce large uncertainties on these derived properties. In addition to these two properties, we derived the hot gas mass,  $M_X = n_e \mu m_p V$ , where  $m_p$  is the proton mass and  $\mu=1.4$  is the mass per proton, the thermal energy  $E_{th} = 3n_e V kT_e$ , and the cooling time  $\tau = E_{th}/L_{bol}$ . Here,  $L_{bol}$  is estimated from the absorption-corrected X-ray hot gas luminosity over the energy range between 0.01–20 keV. The results are listed in Table 2. It has been assumed that the individual temperature components are in pressure equilibrium in order to estimate the electron density and density-

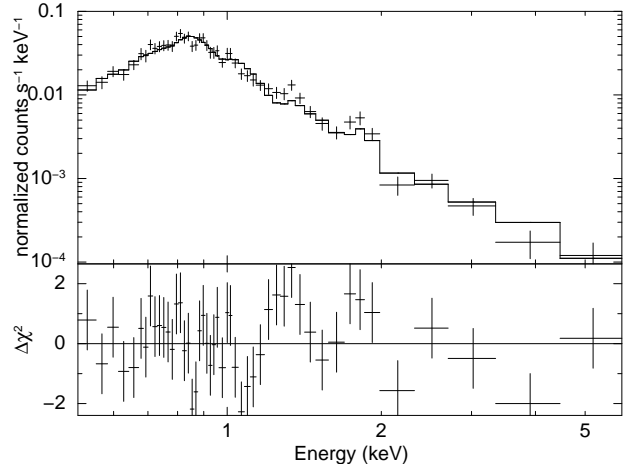


FIG. 6.— Spectrum of the nuclear region defined by  $N_H - kT_e$  correlation of Figure 5. The spectrum was grouped to achieved at least 40 counts in each bin. A background spectrum, extracted from a region to the northeast of the galaxy and outside of the  $D_{25}$  isophote, has been subtracted. An absorbed three temperature component **mekal** model with solar metal abundances is shown as the solid curve. The lower panel shows the contributions to the  $\chi^2$  fit statistic.

dependent properties.

Finally, the X-ray spectral properties of the central region of NGC 2903 can be compared to the properties previously reported by Pérez-Ramírez et al. (2010) using a deep *XMM-Newton* observation. *XMM-Newton* cannot resolve the point sources. Therefore, we fitted the *Chandra* spectrum of the central  $15''$  radius region including point sources. The best-fit model to the *XMM-Newton* data is of an absorbed power law plus thermal component, **phabs(powerlaw+mekal)**, with power law  $\Gamma=2.1$ ,  $kT_e = 0.5$  keV, and  $L_{X(0.5-8 \text{ keV})} = 2.3 \times 10^{39} \text{ erg s}^{-1}$ , (Pérez-Ramírez et al. 2010). The *Chandra* spectrum has higher luminosity,  $L_{X(0.5-8 \text{ keV})} = 3.2 \times 10^{39} \text{ erg s}^{-1}$  and is characterized better with a combination of absorbed disk blackbody and thermal models, **phabs(diskbb+mekal)**, with  $kT_{in} = 1.3$  keV and  $kT_e = 0.5$  keV. When a power-law model is used instead of a disk blackbody, the fitted power law index is lower than for the *XMM-Newton* observation,  $\Gamma = 1.8$ , again driven by the hard X-ray spectral shape. Both spectra suggest the absorption column is very low, at the Galactic value, and that the hot gas temperature is higher than that of the map we derived in the previous section. Note that the diffuse emission only accounts for about 1/3 of the total luminosity in the *Chandra* data (cf. Table 1) with the remainder contributed by point-like sources. The largest contribution,  $L_{X(0.5-8 \text{ keV})} = 1.4 \times 10^{39} \text{ erg s}^{-1}$ , is from CXOJ023210.1+213008, which is also fitted well with a disk blackbody model (see the Appendix) with  $kT_{in}=1.03$  keV. Since X-ray binaries tend to dominate the luminous X-ray point-source population and they are often time variable, the difference in luminosity estimated here compared to the *XMM-Newton* results of Pérez-Ramírez et al. (2010) may be due simply to variability in one or more of these bright X-ray point sources.

### 3.2. Extended Diffuse X-ray Emission

Following the results of § 2.2.2, we divided the low surface brightness diffuse emission surrounding the nu-

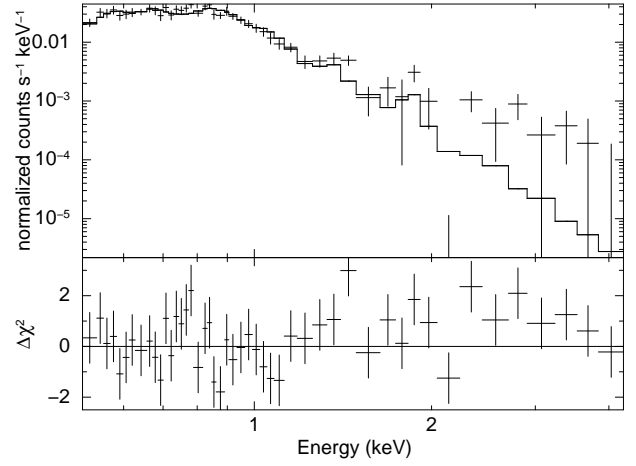
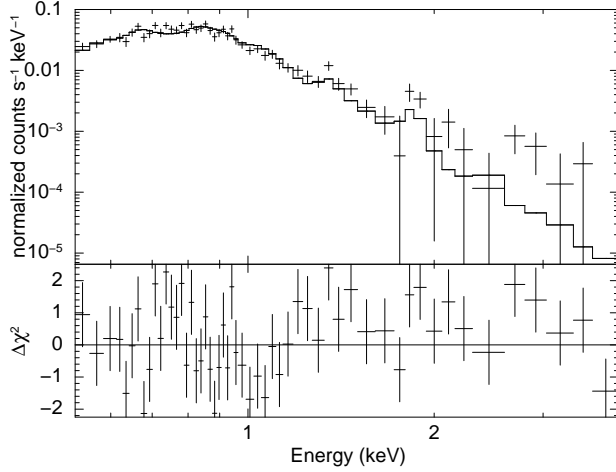


FIG. 7.— Spectra of the east (left) and west (right) side of the low surface brightness diffuse emission regions fitted with the absorbed two temperature models and their the delta  $\chi^2$ .

TABLE 1  
FIT PARAMETERS OF X-RAY DIFFUSE EMISSION

Parameter	Nucleus	West	East
Net count	2448±49	1928±53	2512±61
Fitted energy range (keV)	0.5–6.0	0.5–4.0	0.5–4.0
$n_{\text{H}}/10^{22}$ (cm $^{-2}$ )	0.14 $^{+0.04}_{-0.03}$	0.20 $^{+0.06}_{-0.06}$	0.27 $^{+0.05}_{-0.05}$
$kT_{e1}$ (keV)	0.18 $^{+0.02}_{-0.02}$	0.18 $^{+0.01}_{-0.01}$	0.19 $^{+0.01}_{-0.01}$
$K_1/10^{-4}$	0.38 $^{+0.23}_{-0.27}$	1.58 $^{+0.10}_{-0.07}$	2.57 $^{+1.32}_{-0.89}$
$kT_{e2}$ (keV)	0.55 $^{+0.02}_{-0.02}$	0.55 $^{+0.04}_{-0.04}$	0.56 $^{+0.03}_{-0.03}$
$K_2/10^{-4}$	0.36 $^{+0.08}_{-0.07}$	0.28 $^{+0.05}_{-0.05}$	0.44 $^{+0.07}_{-0.06}$
$kT_{e3}$ (keV)	3.63 $^{+0.81}_{-0.56}$		
$K_3/10^{-4}$	0.30 $^{+0.03}_{-0.03}$		
$\chi^2/\text{dof}$	60.1/42	59.2/41	75.36/49
$L_{\text{X}0.5-8.0}^{\text{abs}}/10^{38}$ (erg s $^{-1}$ )	10.8 $^{+1.1}_{-3.9}$	7.7 $^{+0.0}_{-1.4}$	9.8 $^{+0.0}_{-1.2}$
$L_{\text{X}0.5-8.0}^{\text{int}}/10^{38}$ (erg s $^{-1}$ )	17.9	140	194

TABLE 2  
PROPERTIES OF X-RAY DIFFUSE EMISSION

Parameter	Nucleus	West	East
Volume [ $f$ ] (10 $^{63}$ cm $^3$ )	9.6	56	67
$n_e[f^{-1/2}]$ (cm $^{-3}$ )	1.07, 0.36, 0.06	0.08, 0.03	0.10, 0.03
$P/k[f^{-1/2}]$ (10 $^5$ K cm $^{-3}$ )	46.9	3.5	4.3
$E_{\text{th}}[f^{+1/2}]$ (10 $^{53}$ erg)	93.5	40.4	57.2
$M_{\text{X}}[f^{+1/2}]$ (10 $^5 M_{\odot}$ )	7.6	32.1	44.5
$\tau$ (Myr)	63.2	6.6	13.0

clear zone into two regions, namely the (roughly) east and west zones based on the  $N_{\text{H}} - kT_e$  correlation map shown in Figure 5. These zones do not show strong correlations with the underlying galactic structures seen at other wavelengths. However, the locations of dust lanes relative to the (optical) starlight from the spiral arms (e.g., the SDSS composite image of Figure 1) suggest the eastern region lies closer along our line of sight than the western region. Importantly, if some of the extended (non-nuclear) hot gas diffuse emission lies above (below) the plane of the galaxy, then we would expect the relative absorbing column density to be lower (higher) in the west (east) zone. This is indeed what is deduced from

the thermodynamic maps used to define these two zones (Figure 5).

In order to compare to the hot gas in the nuclear starburst region, the same sequence of models were applied to the hot gas spectra in the east and west zones as was done for the nuclear region with abundances of the thermal component fixed to solar.

We first applied the same single-temperature absorbed thermal model as used for the thermodynamic map over the same energy range. The spectra were grouped to have at least 40 counts in each bin, and  $\chi^2$  statistic is used. The same background spectrum that was used above was applied.

Again, we have reproduced consistent results, specifically  $N_{\text{H}} = (4.6 \pm 0.03) \times 10^{21}$  cm $^{-2}$  and  $kT_e = 0.21 \pm 0.01$  keV for the east region, and  $N_{\text{H}} = (4.3 \pm 0.03) \times 10^{21}$  cm $^{-2}$  and  $kT_e = 0.19 \pm 0.01$  keV for the west region. Likewise, the fitting statistics are not acceptable ( $\chi^2_{\nu} > 2$ ) with larger number counts in the source spectra. Again, there is some emission above 2 keV, hence we expanded the energy range to 0.5–4.0 keV for subsequent spectral analysis.

In both zones, including the higher energy range data did not change the fitting results significantly when fitting to a single-temperature thermal model with solar abundance.

Adding a second component (either power law or second thermal component) improved the fit statistic ( $\chi^2_{\nu} \sim 1.4$ ) in both the zones. However, the best-fitting power law indices in both zones are  $\Gamma \sim 3.7$ . Such steep slopes are unphysical for unresolved point sources. Therefore, we applied two-component thermal models. The fitting results are listed in Tables 1 and 2 and the observed data, spectral model, and fit residuals are shown in Figure 7. Adding a third thermal model component did not improve the fit according to the F-test.

The best-fit temperatures are  $\sim 0.2$  keV and  $\sim 0.6$  keV, which are consistent with the two lower temperatures in the nuclear zone and with typical star-forming regions and the halos of starburst galaxies (Strickland et al. 2004; Yukita et al. 2010). The dominant contribution is from the lower-temperature component, which is consistent with the single-temperature model. Adding a sec-

ond temperature component lowers the absorbing column densities in the two zones with  $N_{\text{H}}$  in the eastern zone slightly higher than in the western zone though they agree within errors.

#### 4. THE NUCLEAR STARBURST AND A SEARCH FOR AN ACTIVE NUCLEUS

Images of the nuclear region in several wavelengths are shown in Figure 8. Each image is  $30'' \times 30''$  centered at R.A. =  $9^{\text{h}}32^{\text{m}}10^{\text{s}}.1$ , decl. =  $21^{\circ}30'03''$ . The emission is rather patchy at most wavelengths but a rough ring-like structure,  $\sim 650$  pc in diameter, has been reported in the literature (e.g., Alonso-Herrero et al. 2001). Although the size of the ring is debated as one-half this size even after deprojection (Comerón et al. 2010). The  $24 \mu\text{m}$  image has the lowest resolution,  $\sim 5''$ . The  $24 \mu\text{m}$  flux is dominated by the star-forming regions to the north of the center. The  $8 \mu\text{m}$  image shows more of a ring-like morphology and is similar to comparable-resolution radio images (not shown; see, e.g., Wynn-Williams & Becklin 1985). The *HST*/NICOMS  $1.6 \mu\text{m}$  and *HST*/ACS F814W images show the numerous star clusters present. The F814W image also reveals that there are complex dust lanes in the east side of the nuclear starburst region. The  $\text{H}\alpha$  image also reveals the ring-like morphology (Alonso-Herrero et al. 2001) consisting of many HII regions.

The high resolution *Chandra* image of the nuclear region reveals that there are a number of point-like sources embedded in the soft X-ray diffuse emission. Most do not correlate spatially with features visible at comparable resolution at other wavelengths as expected if these sources are X-ray binaries. Overall, the X-ray morphology does not trace the ring-like shape but is center-filled and circular rather than the elliptical shapes seen at other wavelengths that roughly match the inclination of the galaxy. The soft X-ray diffuse emission seems to be affected by the dust lanes, showing less emission from the east side of the center and more absorption, appearing green in the tri-color image on the east edge of the starburst region where the strong dust lane can be seen.

As Figure 8 shows, the mass center of NGC 2903 is not well defined because of complex structures and the lack of an obvious active galactic signature. NASA/IPAC Extragalactic Database lists the galactic center as R.A. =  $9^{\text{h}}32^{\text{m}}10^{\text{s}}.11$ , decl. =  $21^{\circ}30'03''.0$ , which is obtained from the Two Micron All Sky Survey. Trachternach et al. (2008) estimated the galactic center position by fitting tilted-ring models to velocity fields derived from HI observations (R.A. =  $9^{\text{h}}32^{\text{m}}10^{\text{s}}.0$ , decl. =  $21^{\circ}30'02''.5$ ), by fitting ellipses to the surface brightness of the *Spitzer*  $3.6 \mu\text{m}$  image (R.A. =  $9^{\text{h}}32^{\text{m}}10^{\text{s}}.1$ , decl. =  $21^{\circ}30'04''.9$ ), and by the location of a point source detected in the radio continuum (R.A. =  $9^{\text{h}}32^{\text{m}}10^{\text{s}}.1$ , decl. =  $21^{\circ}30'04''.3$ ). We carefully registered the *HST*/ACS image to the 2MASS coordinates but found none of the bright star clusters or ionized regions are coincident with any of these four positions. No individual X-ray point sources are detected at any of the four positions either.

We place an upper limit X-ray luminosity for any undetected source in the nuclear region using  $1''$  source extraction radii. The extinction toward the nuclear region is relatively moderate, reportedly ranging from  $A_{\text{V}} \sim 2 - 4$  mag (Alonso-Herrero et al. 2001; Quillen

& Yukita 2001) for the HII regions to  $A_{\text{V}} \sim 5.8$  mag (Alonso-Herrero et al. 2001) for the average over the full  $14''$  diameter nuclear region corresponding to hydrogen column densities of  $(4.6 - 11.2) \times 10^{21} \text{ cm}^{-2}$  based on the standard Galactic gas-to-dust ratio  $N_{\text{H}}/A_{\text{V}} = 1.9 \times 10^{21} \text{ cm}^{-2} \text{ mag}^{-1}$  (Maiolino et al. 2001, and references therein). (Note these values are considerably higher than our best-fit values derived from fits to the X-ray spectra of the nuclear region.) A recent high resolution CO observation indicates that the column density can be as high as  $(6 \pm 3) \times 10^{22} \text{ cm}^{-2}$  (P.-Y. Hsieh, private communication, 2011). Therefore, we assume a column density of  $10^{22} \text{ cm}^{-2}$  to estimate a conservative upper limit X-ray luminosity from an undetected point source. Assuming a power law spectral index of  $\Gamma = 1.7$ , the 90% confidence upper limit luminosity from our *Chandra* observation is  $\sim 1.5 \times 10^{38} \text{ erg s}^{-1}$ . This low value is consistent with the lack of any evidence at other wavelengths for an active nucleus.

#### 5. DISCUSSION

The X-ray emission observed by *Chandra* from within the central few minutes of arc of NGC 2903 is composed of both hard-spectrum point-like sources (observed  $L_{\text{X}} \sim 1.9 \times 10^{40} \text{ erg s}^{-1}$  in the 0.5–8.0 keV range) and soft and hard diffuse extended emission (total observed  $L_{\text{X}} \sim 0.3 \times 10^{40} \text{ erg s}^{-1}$ ). The intrinsic luminosity of the detected point sources is about 25% larger based on our spectral fits but the intrinsic luminosity of the soft diffuse component can be a factor  $\sim 20$  higher (Table 1) because the observed spectrum is so soft. The observed diffuse X-ray luminosity from the central 650 pc region alone is  $\sim 10^{39} \text{ erg s}^{-1}$  with about 30% of this amount contributed by a hot component with  $kT_{\text{e}} \sim 3.6$  keV.

Much of the soft diffuse component is likely created by the collective effects of massive star winds and supernovae in star-forming regions located throughout the disk of NGC 2903. We discuss below whether or not the hard diffuse component may be due to a concentrated hot wind fluid emanating from the central starburst region, the possibility of outflow from this region into the halo, and whether or not some portion of the soft diffuse component originates from this outflow.

##### 5.1. Hard Diffuse X-Ray Emission

Strickland & Heckman (2007, 2009) have done a thorough analysis of the X-ray emission from the central region in the nearby starburst galaxy, M82. We find many parallels between the X-ray properties of the central regions of NGC 2903 and those of M82, as given by Strickland & Heckman, with the notable exception that NGC 2903 does not so readily display copious galactic winds as does M82. Part of the reason is that NGC 2903 is viewed at an inclination of  $60^{\circ}$  compared to the edge-on orientation of M82 but the wind power (or, equivalently, mass loss rate) is apparently much weaker in NGC 2903 compared to M82.

The hard X-ray diffuse emission in M82 is confined to the nuclear starburst region ( $r \sim 500$  pc), whereas the soft X-ray diffuse emission extends into the extraplanar regions above and below the stellar disk. A similar distribution can be seen in NGC 2903. The hard X-ray diffuse emission is only seen in the central  $\lesssim 15''$  (650 pc)

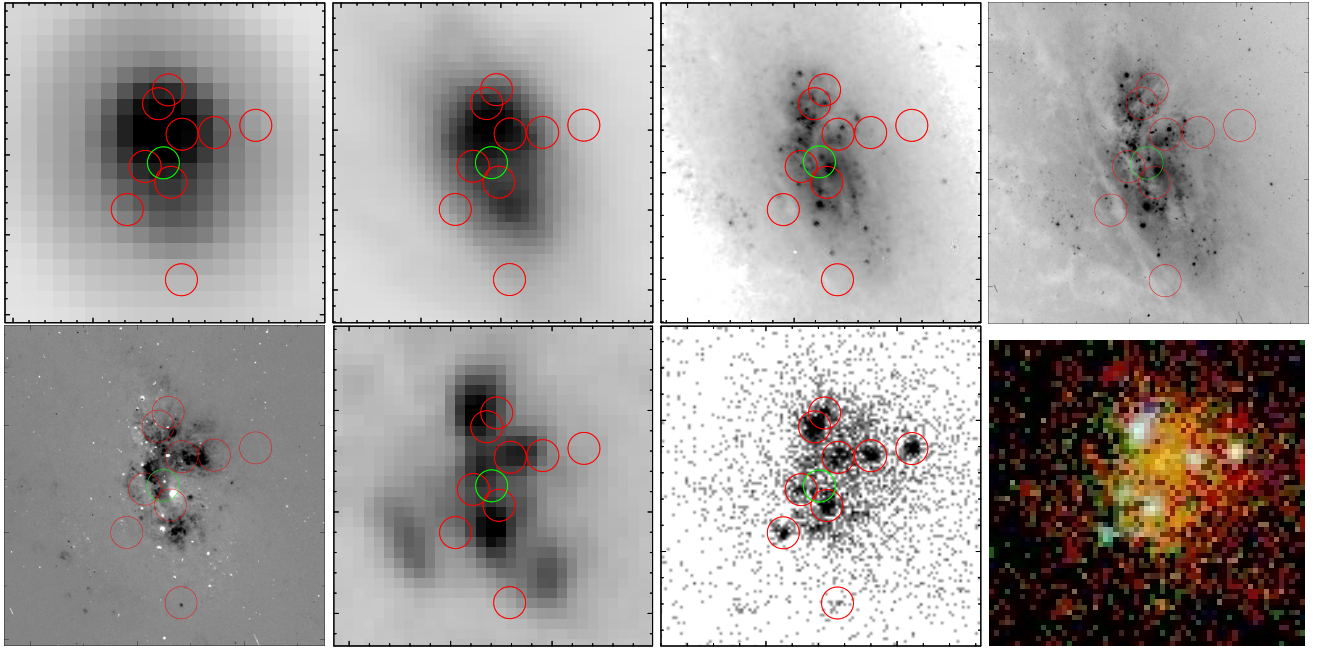


FIG. 8.— Circumnuclear region ( $30'' \times 30''$ ) of NGC 2903. North is up, and east is to the left. Top: (from left to right) the *Spitzer* 24  $\mu\text{m}$ , *Spitzer* 8  $\mu\text{m}$ , *HST*/NICMOS 1.6  $\mu\text{m}$  *HST*/ACS F814W. Bottom: *HST*/ACS continuum-subtracted  $\text{H}\alpha$ , XMM-Newton OM UV, *Chandra* 0.5–8.0 keV X-ray subpixel image, and energy color-coded *Chandra* X-ray image. The X-ray colors indicate the 0.5–1.0 keV (red), 1.0–2.0 keV (green) and 2.0–8.0 keV (blue) energy bands. Red circles indicate the positions of the detected point-like X-ray sources. The green circle depicts the position of the galaxy center as listed in the NASA/IPAC Extragalactic Database. The radius of a circle is  $1''.5$ .

radius nuclear region while the soft X-ray emission extends  $\sim 5$  kpc or more mostly to the north and west of the nucleus. Strickland & Heckman (2007, 2009) also argue that the hard continuum emission is of thermal origin; however, as with NGC 2903, the hard continuum from M82 is formally better fitted with a power law model, so that non-thermal processes such as inverse Compton scattering may contribute to the hard X-ray emission. There are too few net X-ray source counts detected from NGC 2903 to quantify any underlying non-thermal emission component or to use emission lines from highly-ionized metals to better constrain the thermal component of the hard emission as Strickland & Heckman (2007) were able to do for M82.

The hard continuum emission temperature from M82 measured by Strickland & Heckman (2007) is  $\sim 3.6$  keV. This is the same hard-component temperature we found for the nuclear starburst region in NGC 2903. However, the central hot gas pressure deduced from our analysis of the X-ray spectrum is  $5 \times 10^6 \text{ K cm}^{-3}$  whereas Strickland & Heckman (2009) estimate pressures closer to  $10^7$  to  $3 \times 10^7 \text{ K cm}^{-3}$  from models that reproduce the observed hard X-ray luminosity from M82.

Following the notation of Strickland & Heckman (2009), we define the thermalization efficiency,  $\epsilon$ , as the fraction of mechanical energy from star formation that is imparted to (heats) the surrounding gas (the remainder is lost radiatively) and the mass-loading factor,  $\beta$ , as the ratio of the total mass of heated gas to the mass directly ejected by supernovae and stellar winds. The central temperature in a starburst is then (see the review by Veilleux et al. 2005)

$$T_c = 0.4 \frac{\mu m_H \epsilon L_W}{k \beta \dot{M}_W}, \quad (1)$$

where  $\mu = 1.4$  is the mean molecular weight,  $m_H$  the proton mass,  $L_W$  the rate of energy input,  $\dot{M}_W$  the rate of mass ejected from stars and supernovae, and  $k$  is Boltzmann's constant. Furthermore, by equating the rate of energy deposited in the surroundings,  $\epsilon L_W$ , to the asymptotic kinetic energy loss rate,  $(1/2)\beta \dot{M}_W v_\infty^2$ , it follows that the starburst drives a wind with terminal velocity

$$v_\infty^2 = \frac{2\epsilon L_W}{\beta \dot{M}_W} = \frac{5kT_c}{\mu m_H}. \quad (2)$$

Since both  $L_W$  and  $\dot{M}_W$  scale linearly with the SFR,  $T_c$  and  $v_\infty$  are independent of SFR but do depend on the environment through  $\epsilon$  and  $\beta$ . Clearly, both quantities decrease as more cold gas mass is loaded into the wind fluid and as radiative losses increase. Values for  $L_W$  and  $\dot{M}_W$  as a function of time can be taken directly from the Starburst99 (Leitherer et al. 1999) stellar population synthesis models. Using our assumption of solar metallicity and a Salpeter initial mass function (Salpeter 1955) over the stellar mass range  $1\text{--}100 M_\odot$ , and assuming a continuous rate of star formation beginning at some time  $t_o$ ,  $L_W/\dot{M}_W$  is approximately constant after an initial transient phase lasting  $< 20$  Myr so that  $T_c \sim 2.5 \times 10^8 (\epsilon/\beta) \text{ K}$ . Matching this to the observed temperature of the hot component in the nuclear starburst region of NGC 2903,  $(\epsilon/\beta) \sim 0.15$  so that  $v_\infty \sim 3000 (\epsilon/\beta)^{1/2} \sim 1100 \text{ km s}^{-1}$ . For reasonable values of  $\epsilon$  on the range  $0.5\text{--}1.0$  (Veilleux et al. 2005, and references therein) appropriate to the moderate-density central region of NGC 2903, the mass-loading factor is relatively high,  $3.3 < \beta < 6.7$ , compared to typical values derived by Strickland & Heckman (2009) from numerical models for M82 ( $\beta \sim 2.5$ ).

The hard X-ray luminosity scales as  $(\beta \dot{M}_W)^3 / \epsilon R_\star L_W$  (see Strickland & Heckman 2009, for a derivation) where  $R_\star$  is the radius within which the starburst energy and mass are injected. Taking the mean value of  $\beta = 5$  for NGC 2903 and  $\beta = 2.5$  for M82 (Strickland & Heckman 2009), assuming  $\epsilon$  is the same for both galaxies (they likely differ by less than a factor of 2), and noting that  $\dot{M}_W^3 / L_W \propto \text{SFR}^2$ , we can solve for  $R_\star$  for NGC 2903 given the central SFRs and hard X-ray luminosities for the two galaxies and  $R_\star = 300$  pc for M82 (Strickland & Heckman 2009). This gives  $R_\star \sim 780$  pc for the central starburst in NGC 2903 which is close to our estimated size of the star-forming region of 650 pc. Therefore, we conclude that the detected hard X-ray diffuse emission from NGC 2903 is similar to that from M82 suggesting a possible outflow originates from the central starburst provided the current star formation activity has persisted for  $\sim 20$  Myr or longer. This implies the hot wind fluid present in the nuclear region of NGC 2903 dominates the energetics of the flow as is implicit in the original Chevalier & Clegg (1985) model on which the work of Strickland & Heckman (2009) is based. It is natural to ask whether or not the hot gas carries enough energy to escape from the galaxy potential. The escape velocity,  $v_e$ , is roughly 2.6–3.3 times the local circular velocity (e.g., Veilleux et al. 2005). The circular velocity of the inner 7 kpc ( $\sim 6'$ ) in NGC 2903 reaches  $230 \text{ km s}^{-1}$  (de Blok et al. 2008), yielding  $v_e = 600\text{--}760 \text{ km s}^{-1}$ . Therefore, the high-temperature component of the wind fluid is likely to flow outward and eventually to escape from the galaxy disk.

### 5.2. Soft Diffuse X-Ray Emission

Unlike M82, direct detection of any galactic wind emanating from the central regions of NGC 2903 is compromised due to the inclination of the galaxy disk to our line of sight. There is soft diffuse X-ray emission with characteristic temperature 0.2–0.6 keV extending beyond the central starburst with a morphology that does not closely match the underlying structures seen at other wavelengths (§2.2.1). Much of this gas probably originated from supernovae and stellar winds from massive young stars distributed throughout the stellar disk of NGC 2903. Its relatively soft spectrum is likely due to dilution of hotter gas by thermal evaporation of surrounding cold ISM as in the standard model for the formation of interstellar bubbles (Castor et al. 1975; Weaver et al. 1977). However, a portion of this soft X-ray emission may come from a galactic wind, also diluted through mass-loading and further cooled by adiabatic expansion, but lying above the disk of the galaxy.

Based on the thermodynamic maps analyzed in §2.2.2, the soft diffuse X-ray emission can be divided into three distinctive zones, the nuclear, west and east zones. We note that the hydrogen column density is lower in the west than in the east zone and lowest in the nuclear zone. This may suggest the geometry of the hot gas: in the nuclear zone, the gas extends into the lower density halo. The gas in the east zone is mostly confined to within the disk. Because the galaxy is tilted so that the east side is closest to us, any emission from a galactic wind along a line of sight through the east zone would be attenuated by the disk giving the higher  $N_H$  value. Conversely, the

TABLE 3  
PROPERTIES OF X-RAY POINT SOURCES

	R.A. (J2000)	Decl. (J2000)	Counts	S/N	$L_X^a / 10^{38}$ ( $\text{erg s}^{-1}$ )
1	09 31 54.5	21 27 44.6	22.5	3.8	0.25
2	09 31 55.2	21 28 03.3	39.3	5.4	0.44
3	09 31 57.7	21 30 16.5	11.1	2.5	0.08
4	09 31 58.4	21 25 38.0	8.8	2.7	0.10
5	09 31 59.0	21 24 25.3	51.7	6.2	0.58
6	09 31 59.9	21 27 26.6	51.8	6.1	0.58
7	09 32 00.6	21 23 38.5	6.6	2.5	0.07
8	09 32 01.1	21 31 59.2	8.7	2.4	0.06
9	09 32 01.1	21 32 33.7	35.0	5.0	0.39
10	09 32 01.1	21 26 34.4	12.4	3.1	0.09
11	09 32 01.2	21 30 46.5	9.4	2.4	0.07
12	09 32 01.2	21 32 52.0	189.1	12.3	1.40
13	09 32 01.9	21 31 11.1	290.4	15.7	2.12
14	09 32 02.5	21 33 37.5	9.4	3.1	0.07
15	09 32 03.0	21 26 55.1	36.9	5.3	0.41
16	09 32 03.4	21 33 19.8	18.5	3.4	0.14
17	09 32 03.7	21 29 32.9	13.3	3.2	0.10
18	09 32 03.9	21 29 16.7	21.1	3.9	0.15
19	09 32 04.6	21 29 59.9	11.5	3.0	0.09
20	09 32 04.6	21 33 26.6	318.0	16.1	2.35
21	09 32 05.0	21 26 41.4	12.2	2.5	0.14
22	09 32 05.4	21 32 35.0	1043.0	29.5	7.68
23	09 32 06.0	21 28 12.8	157.1	10.8	1.13
24	09 32 06.1	21 28 18.3	7.3	2.5	0.05
25	09 32 06.2	21 30 58.7	2848.3	48.4	20.94
26	09 32 06.3	21 29 57.4	44.5	5.6	0.33
27	09 32 06.6	21 30 04.8	15.9	3.5	0.12
28	09 32 06.9	21 28 34.7	9.9	2.7	0.07
29	09 32 06.9	21 28 55.0	17.0	2.9	0.12
30	09 32 07.2	21 29 36.8	47.9	5.8	0.34
31	09 32 07.4	21 30 55.1	90.5	8.5	0.66
32	09 32 07.6	21 29 02.1	40.7	5.3	0.29
33	09 32 07.7	21 29 56.2	45.1	5.6	0.33
34	09 32 07.9	21 29 30.5	30.6	4.3	0.22
35	09 32 07.9	21 31 44.9	5.9	2.6	0.04
36	09 32 07.9	21 32 13.2	31.2	5.0	0.23
37	09 32 09.1	21 29 09.0	190.9	11.9	1.37
38	09 32 09.5	21 30 06.5	242.0	13.4	1.79
39	09 32 09.6	21 28 49.1	26.0	4.4	0.19
40	09 32 09.7	21 31 06.8	1234.9	32.0	8.95
41	09 32 09.7	21 28 36.9	28.4	4.7	0.20
42	09 32 09.7	21 24 24.1	18.8	3.6	0.21
43	09 32 09.7	21 29 06.3	152.1	10.2	1.09
44	09 32 09.8	21 30 05.8	208.6	10.6	1.54
45	09 32 09.8	21 32 17.2	47.0	6.3	0.35
46	09 32 09.9	21 34 32.5	30.7	4.4	0.23
47	09 32 10.0	21 30 05.7	140.3	6.1	1.04
48	09 32 10.0	21 29 52.0	8.7	2.7	0.06
49	09 32 10.1	21 30 01.2	275.5	13.1	2.03
50	09 32 10.1	21 30 09.8	103.0	5.8	1.15
51	09 32 10.1	21 30 08.5	782.4	22.4	5.82
52	09 32 10.2	21 30 02.7	93.7	5.5	0.69
53	09 32 10.4	21 29 58.6	108.8	8.5	0.80
54	09 32 10.5	21 31 12.0	9.6	2.6	0.07
55	09 32 10.8	21 31 26.4	176.1	12.0	1.31
56	09 32 10.9	21 29 37.7	12.1	2.7	0.09
57	09 32 11.5	21 27 41.7	11.4	3.1	0.08
58	09 32 11.5	21 30 26.1	137.9	10.5	1.02
59	09 32 11.8	21 28 34.9	67.7	7.0	0.49
60	09 32 11.8	21 24 57.3	46.1	5.6	0.52
61	09 32 11.9	21 27 11.2	29.5	4.7	0.21
62	09 32 12.0	21 30 33.9	21.3	4.3	0.15
63	09 32 12.2	21 27 49.6	40.0	5.4	0.29
64	09 32 12.3	21 29 22.9	627.1	21.6	4.59
65	09 32 12.4	21 30 49.5	110.4	9.6	0.82
66	09 32 12.5	21 30 25.9	13.1	3.1	0.09
67	09 32 12.6	21 24 39.9	346.9	15.9	3.91
68	09 32 12.6	21 32 08.1	42.8	6.1	0.31
69	09 32 12.7	21 29 38.8	8.8	2.7	0.07
70	09 32 12.7	21 29 50.3	34.7	5.1	0.26
71	09 32 13.1	21 30 55.8	45.7	6.1	0.33
72	09 32 13.2	21 30 37.4	31.1	4.9	0.23
73	09 32 13.6	21 35 33.0	82.6	7.2	0.61
74	09 32 13.9	21 31 01.2	17.1	3.6	0.13
75	09 32 14.0	21 33 05.2	73.7	7.6	0.54
76	09 32 14.6	21 30 28.6	40.3	5.7	0.30
77	09 32 14.6	21 31 01.2	12.2	3.3	0.09
78	09 32 15.3	21 30 59.0	5.3	2.4	0.04
79	09 32 15.4	21 29 24.9	29.0	4.5	0.21
80	09 32 15.4	21 31 36.9	15.2	3.7	0.11



TABLE 3  
PROPERTIES OF X-RAY POINT SOURCES

	R.A. (J2000)	Decl. (J2000)	Counts	S/N	$L_X/10^{38}$ (erg s $^{-1}$ )
81	09 32 16.4	21 31 11.7	8.9	2.4	0.07
82	09 32 17.3	21 29 46.5	77.8	7.9	0.57
83	09 32 17.7	21 30 20.4	40.5	5.6	0.30
84	09 32 18.9	21 26 36.1	6.5	2.4	0.05
85	09 32 19.6	21 31 05.3	86.0	8.3	0.63
86	09 32 20.0	21 27 48.9	18.1	3.8	0.13
87	09 32 21.0	21 30 02.2	34.7	5.5	0.26
88	09 32 21.6	21 28 20.9	19.3	4.0	0.14
89	09 32 22.2	21 32 41.8	21.9	3.7	0.16
90	09 32 22.9	21 29 24.7	34.6	5.2	0.25
91	09 32 23.0	21 33 02.5	25.1	4.1	0.19
92	09 32 23.6	21 29 13.7	12.5	2.9	0.09

<sup>a</sup> Intrinsic luminosity (0.5–8.0 keV) assuming a power law spectrum of index  $\Gamma = 1.95$ ,  $n_H = 2.9 \times 10^{20}$  cm $^{-2}$ .

hot gas observed along lines of sight through the west zone is likely either (also) from the disk or from the wind located above the disk resulting in a relatively lower absorption column density. This geometry naturally also explains the higher X-ray surface brightness to the west (Figure 2) but does not easily explain the observed hot gas morphology; the shape of the soft diffuse X-ray emission does not approximate the bi-conical outflow seen in M82, for instance.

In any case, the X-ray CCD data alone do not give accurate kinematic information of hot gas. The kinematics of an outflowing gas can be obtained from high-resolution spectroscopic measurements of warm ionized gas. In fact, Hägele et al. (2009) argue that H $\beta$  line structures and properties measured from some nuclear star clusters are akin to those of H $\alpha$  emission in NGC 1569 investigated by Westmoquette et al. (2007b,a) who concluded that these features are indicative of an outflow. Mapping the warm ionized gas in the central region of NGC 2903 will constrain whether or not the hot gas is escaping from the galaxy.

### 5.3. Nuclear Activity

There is no compact source detected coincident with the position of the mass center in NGC 2903. This is consistent with the lack of any AGN signature visible at other wavelengths. We place an upper limit of  $L_{X(0.5-8.0 \text{ keV})} = (1-2) \times 10^{38}$  erg s $^{-1}$  to any undetected point-like nuclear source.

We can infer the mass of the central object from the  $M_{\text{BH}} - \sigma$  relation (Ferrarese & Merritt 2000). The observed stellar velocity dispersion in the nuclear region of NGC 2903 listed in the HYPERLEDA<sup>3</sup> database (Paturel et al. 2003) is  $101.1 \pm 6.8$  km s $^{-1}$  (Héraudeau & Simien 1998). This implies a black hole mass of  $10^6 - 10^7 M_\odot$  (Tremaine et al. 2002; Graham et al. 2011; Graham 2012). Therefore, we take  $10^7 M_\odot$  as an upper limit to the mass of the nucleus. If we assume that the ambient hot gas is spherically accreting onto this central object, the volume-weighted Bondi accretion rate is estimated as  $\dot{M}_{\text{Bondi}} = 5 \times 10^{-8} M_\odot \text{ yr}^{-1}$  using Equation (6) in Soria et al. (2006) and values of the gas temperature and density as listed in Table 2. We emphasize that

this accretion rate only accounts for accretion of the hot phase of gas in the nuclear region.

We define the dimensionless accretion parameter,  $\dot{m}$ , as  $\dot{m} \equiv 0.1 \dot{M} c^2 / L_{\text{Edd}} \equiv \dot{M} / \dot{M}_{\text{Edd}}$ , where  $\dot{M}$  is the accretion rate and  $\dot{M}_{\text{Edd}}$  is the accretion rate that would produce the Eddington luminosity in a radiatively efficient case. For the NGC 2903 nucleus, we obtain  $\dot{m} = 2 \times 10^{-7}$ . In such low radiative efficiency regime, accretion is likely to be advection dominated. From the self-similar solution of Narayan & Yi (1994), the bolometric luminosity is estimated as  $L_{\text{bol}} = \eta \dot{M} c^2 = (10\dot{m}) \dot{M} c^2$ , where  $\eta$  is the radiative efficiency. This leads to the corresponding  $L_{\text{bol}} \sim 10^{34}$  erg s $^{-1}$ . The predicted X-ray luminosity can be a factor of 10 lower than the bolometric luminosity for a supermassive black hole (Elvis et al. 1994), resulting in  $L_X \sim 10^{33}$  erg s $^{-1}$ . A similar  $L_X$  value is also obtained from the  $L_X - \dot{m}$  relation derived by Merloni et al. (2003) for advection models (taking into account that the alternative definition of  $\dot{m} \equiv \dot{M} c^2 / L_{\text{Edd}}$  is used in their paper.) The hot gas component alone can only provide enough accretion to produce  $L_X \sim 10^{33}$  erg s $^{-1}$ .

In general, nuclear black holes in nuclear starburst galaxies are much more active than in NGC 2903 because cold gas is also accreted onto the black hole. There is a tight correlation between nuclear SFR and black hole accretion rate (BHAR) found in Seyfert galaxies (Diamond-Stanic & Rieke 2012). The SFR-BHAR suggests that external cold gas triggers star formation and AGNs or nuclear star formation fuels subsequent AGN activity. The SFR measured from hydrogen recombination lines in the central 15'' (650 pc) region in NGC 2903 is  $0.7 M_\odot \text{ yr}^{-1}$  (Alonso-Herrero et al. 2001). For such an SFR, we would expect  $\dot{M} \sim 0.01 - 0.1 M_\odot \text{ yr}^{-1}$  for the Seyfert galaxies studied by (Diamond-Stanic & Rieke 2012) because the SFR corresponds to a cold gas inflow  $\dot{M}$ . However, given the upper limit to the X-ray luminosity, the cold gas  $\dot{M}$  in NGC 2903 must be much lower,  $\lesssim 3 \times 10^{-5} M_\odot \text{ yr}^{-1}$ , and is inconsistent with the SFR-BHAR correlation, even considering systematic uncertainties among different methods to derive SFRs and accretion rates.

Planesas et al. (1997) estimated an H $_2$  mass of  $1.8 \times 10^8 M_\odot$ , corresponding to a surface density of  $160 M_\odot \text{ pc}^{-2}$  in the nuclear region of NGC 2903. Moreover, the recent high resolution CO image shows a gas structure swirling into the center (P.-Y. Hsieh, private communication). Therefore, there is enough material available in the central region to accrete on to a central massive object in NGC 2903.

We point out that only a small fraction ( $\sim 10\%$ ) of gas fueling nuclear SFR is needed in order to trigger a nuclear activity as luminous as in Seyfert galaxies. In NGC 2903, the 10% of cold gas inflow may be also consumed in the nuclear starburst, heated by massive stars and supernovae, and/or ejected in a galactic outflow.

Support for this work was provided in part by the National Aeronautics and Space Administration through Chandra Award GO0-11099A issued by the *Chandra* X-ray Observatory Center, which is operated by the Smithsonian Astrophysical Observatory for and on behalf of

<sup>3</sup> <http://leda.univ-lyon1.fr>

TABLE 4  
FIT PARAMETERS OF BRIGHT X-RAY POINT SOURCES

Parameter	J09325.4+213235	J093206.2+213058	J093209.7+213106	J093210.1+213008	J093212.3+212922
MeKaL					
$n_{\mathrm{H}}/10^{22}$ (cm $^{-2}$ )	$0.15^{+0.02}_{-0.02}$	$0.14^{+0.01}_{-0.01}$	$0.23^{+0.03}_{-0.03}$	$2.00^{+0.24}_{-0.25}$	$0.12^{+0.04}_{-0.04}$
$kT$ (keV)	$3.05^{+0.38}_{-0.28}$	$3.04^{+0.24}_{-0.24}$	$1.94^{+0.19}_{-0.17}$	$2.31^{+0.35}_{-0.35}$	$7.31^{+3.15}_{-1.87}$
$Z/Z_{\odot}$	$0.00^{+0.10}_{-0.00}$	$0.05^{+0.11}_{-0.05}$	$0.03^{+0.05}_{-0.03}$	$0.14^{+0.25}_{-0.14}$	$0.00^{+0.57}_{-0.00}$
$K/10^{-4}$	$0.82^{+0.05}_{-0.07}$	$2.17^{+0.14}_{-0.12}$	$1.35^{+0.14}_{-0.14}$	$2.29^{+0.07}_{-0.04}$	$0.38^{+0.02}_{-0.5}$
$\chi^2/\mathrm{dof}$	88.9/77	148/156	64.1/90	68.6/67	81.5/50
$f_{\mathrm{X}0.5-8.0\mathrm{keV}}/10^{-14}$ (erg s $^{-1}$ cm $^{-2}$ )	6.67	18.2	7.04	7.44	4.74
Power law					
$n_{\mathrm{H}}/10^{22}$ (cm $^{-2}$ )	$0.25^{+0.02}_{-0.07}$	$0.25^{+0.02}_{-0.07}$	$0.40^{+0.03}_{-0.02}$	$2.62^{+0.32}_{-0.39}$	$0.16^{+0.03}_{-0.06}$
$\Gamma$	$2.26^{+0.07}_{-0.07}$	$2.29^{+0.07}_{-0.06}$	$2.82^{+0.09}_{-0.09}$	$3.04^{+0.29}_{-0.22}$	$1.64^{+0.06}_{-0.08}$
$K/10^{-4}$	$0.27^{+0.03}_{-0.03}$	$0.75^{+0.05}_{-0.05}$	$0.51^{+0.06}_{-0.05}$	$1.68^{+0.87}_{-0.89}$	$0.09^{+0.01}_{-0.01}$
$\chi^2/\mathrm{dof}$	101/78	151/157	73.3/91	70.9/68	85.6/51
$f_{\mathrm{X}0.5-8.0\mathrm{keV}}/10^{-14}$ (erg s $^{-1}$ cm $^{-2}$ )	6.82	18.8	7.17	7.59	5.00
DiskBB					
$n_{\mathrm{H}}/10^{22}$ (cm $^{-2}$ )	$0.05^{+0.02}_{-0.02}$	$0.05^{+0.01}_{-0.01}$	$0.12^{+0.02}_{-0.02}$	$1.61^{+0.38}_{-0.32}$	$0.04^{+0.03}_{-0.03}$
$kT_{\mathrm{in}}$ (keV)	$1.07^{+0.07}_{-0.05}$	$1.01^{+0.04}_{-0.04}$	$0.83^{+0.17}_{-0.04}$	$1.03^{+0.17}_{-0.14}$	$1.41^{+0.17}_{-0.11}$
$K/10^{-4}$	$28.1^{+6.0}_{-6.0}$	$91.4^{+25.1}_{-12.9}$	$94.9^{+24.4}_{-18.9}$	$67.5^{+37.8}_{-23.0}$	$6.03^{+2.02}_{-2.10}$
$\chi^2/\mathrm{dof}$	84.5/78	171/157	68.9/91	68.2/68	73.5/51
$f_{\mathrm{X}0.5-8.0\mathrm{keV}}/10^{-14}$ (erg s $^{-1}$ cm $^{-2}$ )	6.59	17.3	6.89	7.00	4.42
X-ray luminosity					
$L_{\mathrm{X}0.5-8.0\mathrm{keV}}^{\mathrm{int}}/10^{38}$ (erg s $^{-1}$ )	6.64	20.8	9.50	13.8	4.33

NOTE. — Errors are  $1\sigma$  (68% confidence interval) uncertainty. Intrinsic X-ray luminosity is estimated using the best-fit model.

the National Aeronautics Space Administration under K. Wong for fruitful discussions.  
contract NAS8-03060. M.Y. acknowledges R. Buta and

#### APPENDIX

##### X-RAY POINT-SOURCE ANALYSIS

Source positions, number of source counts (corrected for the finite-aperture model PSF), S/N, and estimated source luminosities in the 0.5–8.0 keV range are tabulated in Table 3. The listed source positions are refinements from the initial source detection estimates; refined positions were made by fitting circular Gaussian models to the spatial distribution of X-ray events in the vicinity of each source. The source luminosities were estimated from the average count rate during the observation using the Portable Interactive Multi-Mission Simulator (PIMMS)<sup>4</sup> assuming an absorbed power-law spectral shape with spectral index  $\Gamma = 1.95$  and with a hydrogen column density equal to the Galactic column density along the line of sight of NGC 2903,  $n_{\mathrm{H}} = 2.9 \times 10^{20}$  cm $^{-2}$ , and solar abundances. We note that estimating flux using individual response and effective area files for each source gives more accurate value. However, PIMMS estimation is reasonable here due to low S/N for the most of sources; therefore, the statistical uncertainties are larger than the systematic uncertainties due to differences in the response matrices implemented in PIMMS than those of the actual observation.

Here, the X-ray spectra of the five highest-count sources are analyzed. This includes one source in the nuclear region, CXOUJ093210.1+213008, the source mentioned in § 2.1, and three others. All five are coincident with sources detected with *XMM-Newton* in a 21 April 2009 observation (Pérez-Ramírez et al. 2010) although sources in the nuclear region are highly confused at the *XMM-Newton* resolution (*XMM*-NGC2903 X-1 is 3.9'' distant from CXOUJ093210.1+213008).

Spectral analysis was performed using the XSPEC v.12.6 spectral-fitting package using redistribution matrices and ancillary response files appropriate to the source location on the detector. These files were generated using the CIAO utilities *mkacisrmf*, *mkarf*, and associated programs. Absorbed (XSPEC's **phabs**) power law (**powerlaw**), blackbody accretion disk (**diskbb**), and optically-thin thermal plasma (**mekal**) models were fitted to the observed spectra in the 0.3–10.0 keV range using the  $\chi^2$  fit statistic (events were grouped to ensure a minimum of 10 counts per spectral energy bin). Results of the fitting are given in Table 4 and the observed and model spectra and delta  $\chi^2$  are displayed in Figure 9. The intrinsic (absorption-corrected) 0.5–8.0 keV luminosities of these sources, as estimated using the best-fitting model, are listed in the bottom row of Table 4.

<sup>4</sup> <http://heasarc.nasa.gov/docs/software/tools/pimms.html>

Three sources are best fit using the blackbody-disk model. This model is typically applied to accreting X-ray binary systems. The `diskbb` model results in inner disk temperatures of  $T_{\text{in}} \sim 1$  keV as expected for stellar-mass black holes (e.g., Remillard & McClintock 2006). The most luminous source, CXOUJ093206.2+213058, and the source located in the bright star-forming region, CXOUJ093209.7+213106, are best fit using a thermal emission model indicative of hot gas. Note, however, that the best-fitting abundances for these (and for the other three) sources are much less than the solar value due to the lack of observed line features. Furthermore, the resulting plasma temperatures are much higher than is typical of diffuse hot gas in nearby spiral galaxies such as NGC 2903. These results suggest that these two sources may also be accreting X-ray binaries. The source in the nuclear region has by far the highest intervening column density. This absorbing material is likely local to the nuclear region.

## REFERENCES

- Alonso-Herrero, A., Ryder, S. D., & Knapen, J. H. 2001, *MNRAS*, 322, 757
- Anders, E., & Grevesse, N. 1989, *Geochim. Cosmochim. Acta*, 53, 197
- Athanassoula, E. 1992, *MNRAS*, 259, 345
- Buta, R. J. 2011, arXiv:1102.0550
- Castor, J., McCray, R., & Weaver, R. 1975, *ApJ*, 200, L107
- Chevalier, R. A., & Clegg, A. W. 1985, *Nature*, 317, 44
- Chung, A., van Gorkom, J. H., Kenney, J. D. P., Crowl, H., & Vollmer, B. 2009, *AJ*, 138, 1741
- Combes, F., & Elmegreen, B. G. 1993, *A&A*, 271, 391
- Comerón, S., Knapen, J. H., Beckman, J. E., et al. 2010, *MNRAS*, 402, 2462
- Davies, R. I., Hicks, E., Schartmann, M., et al. 2010, in *IAU Symposium*, Vol. 267, IAU Symposium, 283–289
- de Blok, W. J. G., Walter, F., Brinks, E., et al. 2008, *AJ*, 136, 2648
- Diamond-Stanic, A. M., & Rieke, G. H. 2012, *ApJ*, 746, 168
- Dickey, J. M., Hanson, M. M., & Helou, G. 1990, *ApJ*, 352, 522
- Drozdovsky, I. O., & Karachentsev, I. D. 2000, *A&AS*, 142, 425
- Elvis, M., Wilkes, B. J., McDowell, J. C., et al. 1994, *ApJS*, 95, 1
- Ferrarese, L., & Merritt, D. 2000, *ApJ*, 539, L9
- Graham, A. W. 2012, *MNRAS*, 422, 1586
- Graham, A. W., Onken, C. A., Athanassoula, E., & Combes, F. 2011, *MNRAS*, 412, 2211
- Hägele, G. F., Díaz, Á. I., Cardaci, M. V., Terlevich, E., & Terlevich, R. 2009, *MNRAS*, 396, 2295
- Helfer, T. T., Thornley, M. D., Regan, M. W., et al. 2003, *ApJS*, 145, 259
- Héraudeau, P., & Simien, F. 1998, *A&AS*, 133, 317
- Hernandez, O., Carignan, C., Amram, P., Chemin, L., & Daigle, O. 2005, *MNRAS*, 360, 1201
- Higdon, J. L., Buta, R. J., & Purcell, G. B. 1998, *AJ*, 115, 80
- Irwin, J. A., Hoffman, G. L., Spekkens, K., et al. 2009, *ApJ*, 692, 1447
- Knapen, J. H., Pérez-Ramírez, D., & Laine, S. 2002, *MNRAS*, 337, 808
- Kormendy, J., & Kennicutt, Jr., R. C. 2004, *ARA&A*, 42, 603
- Leitherer, C., Schaerer, D., Goldader, J. D., et al. 1999, *ApJS*, 123, 3
- Leon, S., Jeyakumar, S., Pérez-Ramírez, D., et al. 2008, *A&A*, 491, 703
- Levenson, N. A., Weaver, K. A., Heckman, T. M., Awaki, H., & Terashima, Y. 2004, *ApJ*, 602, 135
- Li, J., Kastner, J. H., Prigozhin, G. Y., et al. 2004, *ApJ*, 610, 1204
- Maiolino, R., Marconi, A., Salvati, M., et al. 2001, *A&A*, 365, 28
- Martin, P., & Friedli, D. 1997, *A&A*, 326, 449
- Masters, K. L., Nichol, R. C., Hoyle, B., et al. 2011, *MNRAS*, 411, 2026
- Maughan, B. J., Ellis, S. C., Jones, L. R., et al. 2006, *ApJ*, 640, 219
- Merloni, A., Heinz, S., & di Matteo, T. 2003, *MNRAS*, 345, 1057
- Morgan, W. W. 1958, *PASP*, 70, 364
- Narayan, R., & Yi, I. 1994, *ApJ*, 428, L13
- O’Sullivan, E., Vrtilik, J. M., Kempner, J. C., David, L. P., & Houck, J. C. 2005, *MNRAS*, 357, 1134
- Paturol, G., Petit, C., Prugniel, P., et al. 2003, *A&A*, 412, 45
- Pérez-Ramírez, D., Caballero-García, M. D., Ebrero, J., & Leon, S. 2010, *A&A*, 522, A53+
- Pérez-Ramírez, D., Knapen, J. H., Peletier, R. F., et al. 2000, *MNRAS*, 317, 234
- Pilyugin, L. S., Vilchez, J. M., & Contini, T. 2004, *A&A*, 425, 849
- Planesas, P., Colina, L., & Perez-Olea, D. 1997, *A&A*, 325, 81
- Popping, G., Pérez, I., & Zurita, A. 2010, *A&A*, 521, A8+
- Quillen, A. C., & Yukita, M. 2001, *AJ*, 121, 2095
- Randall, S., Nulsen, P., Forman, W. R., et al. 2008, *ApJ*, 688, 208
- Remillard, R. A., & McClintock, J. E. 2006, *ARA&A*, 44, 49
- Salpeter, E. E. 1955, *ApJ*, 121, 161
- Sarzi, M., Allard, E. L., Knapen, J. H., & Mazzuca, L. M. 2007, *MNRAS*, 380, 949
- Sellwood, J. A. 1993, *PASP*, 105, 648
- Sérsic, J. L., & Pastoriza, M. 1965, *PASP*, 77, 287
- . 1967, *PASP*, 79, 152
- Sheth, K., Vogel, S. N., Regan, M. W., et al. 2002, *AJ*, 124, 2581
- Shlosman, I. 1999, in *Astronomical Society of the Pacific Conference Series*, Vol. 187, The Evolution of Galaxies on Cosmological Timescales, ed. J. E. Beckman & T. J. Mahoney, 100–114
- Shlosman, I., Begelman, M. C., & Frank, J. 1990, *Nature*, 345, 679
- Soria, R., Fabbiano, G., Graham, A. W., et al. 2006, *ApJ*, 640, 126
- Strickland, D. K., & Heckman, T. M. 2007, *ApJ*, 658, 258
- . 2009, *ApJ*, 697, 2030
- Strickland, D. K., Heckman, T. M., Colbert, E. J. M., Hoopes, C. G., & Weaver, K. A. 2004, *ApJS*, 151, 193
- Swartz, D. A., Yukita, M., Tennant, A. F., Soria, R., & Ghosh, K. K. 2006, *ApJ*, 647, 1030
- Tennant, A. F. 2006, *AJ*, 132, 1372
- Thompson, T. A., Quataert, E., & Murray, N. 2005, *ApJ*, 630, 167
- Trachternach, C., de Blok, W. J. G., Walter, F., Brinks, E., & Kennicutt, R. C. 2008, *AJ*, 136, 2720
- Tremaine, S., Gebhardt, K., Bender, R., et al. 2002, *ApJ*, 574, 740
- Tsai, C.-W., Turner, J. L., Beck, S. C., et al. 2006, *AJ*, 132, 2383
- Tschöke, D., Hensler, G., & Junkes, N. 2003, *A&A*, 411, 41
- Tyler, K., Quillen, A. C., LaPage, A., & Rieke, G. H. 2004, *ApJ*, 610, 213
- Veilleux, S., Cecil, G., & Bland-Hawthorn, J. 2005, *ARA&A*, 43, 769
- Walter, F., Brinks, E., de Blok, W. J. G., et al. 2008, *AJ*, 136, 2563
- Wang, J., Fabbiano, G., Elvis, M., et al. 2009, *ApJ*, 694, 718
- Watabe, Y., Kawakatu, N., & Imanishi, M. 2008, *ApJ*, 677, 895
- Weaver, K. A., Heckman, T. M., & Dahlem, M. 2000, *ApJ*, 534, 684
- Weaver, R., McCray, R., Castor, J., Shapiro, P., & Moore, R. 1977, *ApJ*, 218, 377
- Westmoquette, M. S., Exter, K. M., Smith, L. J., & Gallagher, J. S. 2007a, *MNRAS*, 381, 894
- Westmoquette, M. S., Smith, L. J., Gallagher, J. S., & Exter, K. M. 2007b, *MNRAS*, 381, 913
- Wynn-Williams, C. G., & Becklin, E. E. 1985, *ApJ*, 290, 108
- York, D. G., Adelman, J., Anderson, Jr., J. E., et al. 2000, *AJ*, 120, 1579
- Yukita, M., Swartz, D. A., Tennant, A. F., & Soria, R. 2010, *AJ*, 139, 1066

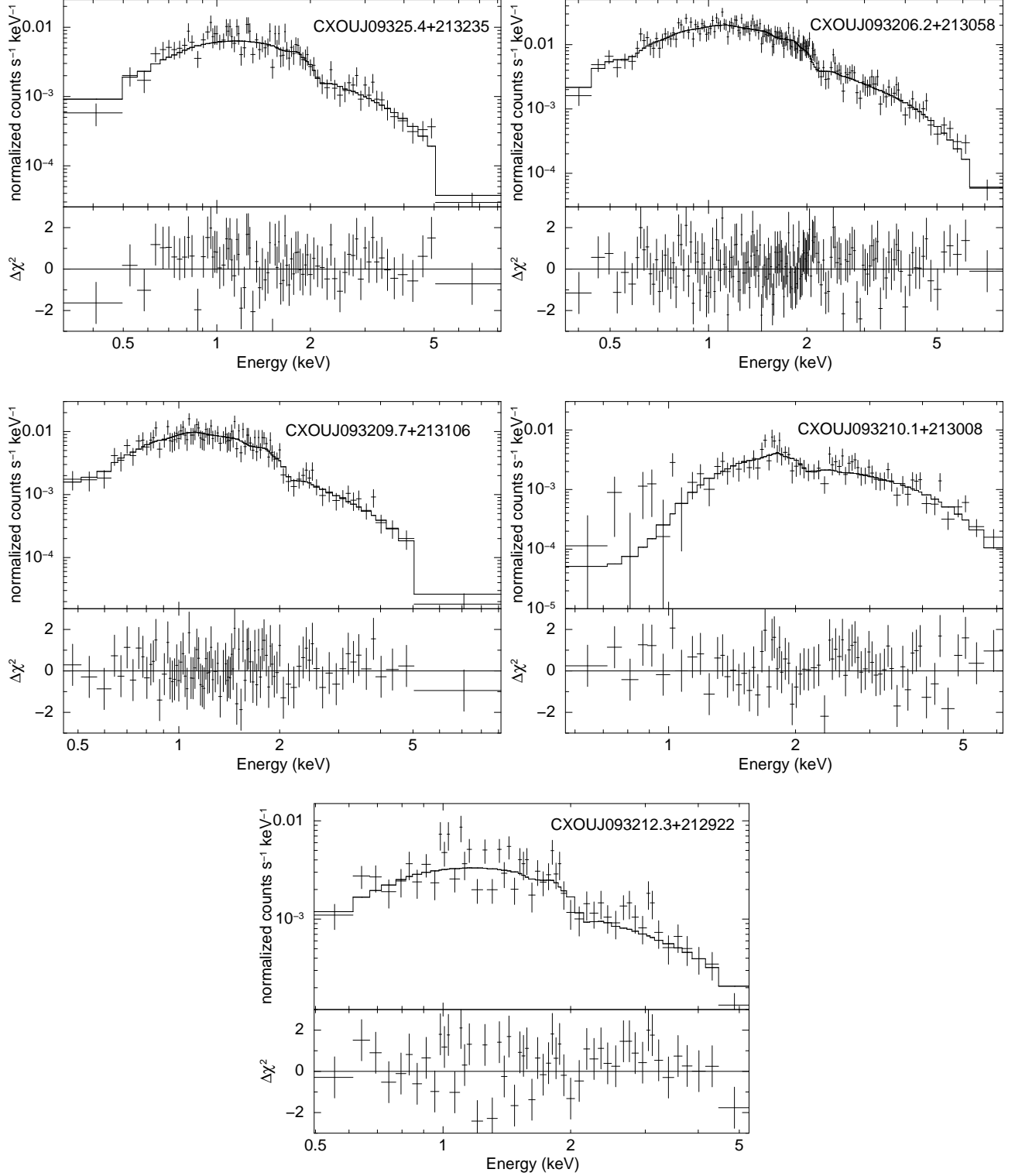


FIG. 9.— Spectra, best-fitting models (solid histogram), and fit residuals (lower panel) of the brightest sources in NGC 2903 detected in the *Chandra* observation taken on March 7, 2010. Details of all model fits including fit parameters and X-ray fluxes estimated from model fits are listed in Table 4.